

Characterization of quantum states of light by means of
homodyne detection and reconstruction of Wigner
functions

Thesis by
Andrés Martínez Silva

In Partial Fulfillment of the Requirements for the
Degree of
Bachelor of Science in Physics

Supervised by
Prof. Alejandra Valencia, Ph.D.



UNIVERSIDAD DE LOS ANDES
Bogotá, Colombia

2020
Defended July 27

© 2020

Andrés Martínez Silva
ORCID: 0000-0002-1261-9906

All rights reserved

ACKNOWLEDGEMENTS

I would like to offer my special thanks to Professor Alejandra Valencia for the guidance during the realization of this work, for the passion she placed and for the patience she had during the way. I am grateful to all the members of the Quantum Optics Group at Universidad de Los Andes for always being willing to help me, especially with those who worked by my side in the lab. I also thank my friends who were my moral support and who pushed me to go further. Last but not least, I thank my family especially my parents because this work was only possible due to their faith in me, they are my inspiration.

ABSTRACT

In this work, a continuous variable quantum tomography is presented. This is done using two approaches, one using simulated data and another one using data from measurements performed in the laboratory. The Radon inverse transform, under the approximation of filtered back projection, alongside the details on the implementation of balanced homodyne detection needed to perform the tomography are clearly explained. Density matrices in the quadrature and number representation are also obtained from the Wigner function. Additionally, complete documentation of the computational implementation and a user-friendly interface for the tomography is reported.

En este trabajo, se presenta una tomografía cuántica en variables continuas. Esto se realiza utilizando dos enfoques, uno con datos simulados y otro con datos de mediciones realizadas en el laboratorio. La transformación inversa del radón, bajo la aproximación de retroproyección filtrada, junto con los detalles sobre la implementación de la detección homodina balanceada necesaria para realizar la tomografía se explican claramente. Las matrices densidad en representación de cuadraturas y Fock también se obtienen de la función Wigner. Además, la documentación completa sobre la implementación computacional de la tomografía y una interfaz gráfica fácil de usar son reportadas.

TABLE OF CONTENTS

Acknowledgements	iii
Abstract	iv
Table of Contents	v
List of Illustrations	vi
Chapter I: Introduction	1
Chapter II: Theory	4
2.1 Quadrature representation	4
2.2 Balanced homodyne detection	7
2.3 Quantum states of light	11
2.4 Wigner function	18
2.5 Quantum tomography	20
Chapter III: Computational simulations	24
3.1 Data generation	24
3.2 Wigner reconstruction via quantum tomography	28
3.3 Density matrix recuperation	32
Chapter IV: Experiment	42
4.1 Optical set-up	42
4.2 Electronic set-up	43
4.3 Measurements	44
4.4 Tomography	47
Chapter V: Conclusions and perspectives	49
Bibliography	50
Appendix A: Computational implementation	53
A.1 Data generation	53
A.2 Tomography	56
A.3 Density matrix calculation	59
Appendix B: GUI	64

LIST OF ILLUSTRATIONS

<i>Number</i>	<i>Page</i>
2.1 The phasor diagram for an electric field with phase ϕ and magnitude \mathcal{E}_0 [2].	6
2.2 Phasor diagram for quadratures X_1 and X_2 considering their uncertainty [2].	7
2.3 Schematic for homodyne detection. LO is the local oscillator and S the field that is going to be characterized. PS allows phase shifting in the LO and the subtracted current i_- yields the quadratures of S.	8
2.4 Phasor diagram for a coherent state with amplitude α and phase ϕ . $\Delta q = \Delta p$ and follow the relation on Eq. [2.17]	13
2.5 Density matrix ρ_{nm} for a coherent state with an amplitude $\alpha = 3$	14
2.6 Phasor diagram for a thermal state. This state is centered in zero, as on average it has no amplitude, and uncertainty on both quadratures is equal. It is not a minimum uncertainty state.	15
2.7 Density matrix ρ_{nm} for a thermal state with $\beta = 0.2$. This matrix is a statistical mixture, therefore the matrix is diagonal.	15
2.8 Phasor diagram for the vacuum state. As expected it is centered at the origin zero, as on average it has no amplitude. As a minimum-uncertainty state Δp and Δq follow the relation on Eq. (2.17)	16
2.9 Density matrix ρ_{nm} for the vacuum state according to Eq. (2.50) using $\alpha = 0$. The vacuum state is a state with zero photons.	16
2.10 Phasor diagram for the vacuum squeezed state (a), phase squeezed states (b) and amplitude squeezed states (c). The uncertainty relationship for these states complies with the uncertainty principle in Eq. (2.17), but is not evenly distributed.	17
2.11 Density matrix ρ_{nm} for the squeezed vacuum state with a squeezing factor of 2 and $\theta = 0$. This matrix only has non zero values on even values of n and m	18
2.12 Wigner functions for multiple states obtained using the analytical solution.	20

2.13 Wigner function $W(q, p)$ and its projections, the quadrature distributions $pr(x, \phi)$. The Radon inverse transform allows reconstruction of the Wigner function from its projections. Adapted from Ref. [19].	22
3.1 Process for obtaining simulated quadrature distributions. A normal distribution is sampled and then fitted. (a) are ten thousand random samples following a normal distribution with $\mu = 5$ and $\sigma = 1$. They can be interpreted as measurements of $i_1 - i_2$ over time. (b) resembles data from (a) in a histogram of 100 bins and the corespondent gaussian fit over the data. This fit would be used as the quadrature distribution for a given phase ϕ . The fit yields a gaussian with $\mu = 4.976$ and $\sigma = 0.977$	25
3.2 Simulated quadrature distributions for the vacuum state, using $\mu = 0$ and $\sigma = \frac{1}{\sqrt{2}}$ for every phase. By looking at the peaks it is evident that they are not equal, this accounts for the randomness introduced during the simulation process. Only 25 of the 100 simulated phases are portrayed.	26
3.3 Simulated quadrature distributions for the thermal state using $\sigma = 3$. Only 25 of the 100 simulated phases are portrayed.	27
3.4 Simulated quadrature distributions for a coherent state with real and imaginary equal amplitudes $Re(\alpha) = Im(\alpha) = 3$. From above (b) it can be seen that the distributions follow a sinusoidal pattern.	27
3.5 Simulated quadrature distributions for the squeezed vacuum using $\eta = 3\pi/4$ (a), squeezed vacuum using $\eta = \pi/4$ (b) and the squeezed amplitude coherent state using $\eta = \pi/2$ and $Re(\alpha) = Im(\alpha) = 3$	28
3.6 Side view of the simulated squeezed vacuum in Fig. [3.5], the sinusoidal height of the peaks is evident from this perspective.	29
3.7 Wigner function for the vacuum state reconstructed via quantum tomography over simulated quadrature marginal distributions. A cutoff frequency $k_c = 5$ was used.	30
3.8 Wigner function for coherent state reconstructed via quantum tomography over simulated quadrature marginal distributions. In this case, both quadratures have the same value. A cutoff frequency $k_c = 5$ was used.	31
3.9 Wigner function for simulated coherent states with only real (b) or imaginary (a) amplitudes. Both were reconstructed using $k_c = 5$	31

3.10 Wigner function for thermal state reconstructed via quantum tomography over simulated quadrature marginal distributions. The function is centered at the origin. A cutoff frequency $k_c = 1$ was used to perform the tomographic process.	32
3.11 Wigner functions for the squeezed vacuum reconstructed via quantum tomography over simulated quadrature marginal distributions. All the functions are centered at the origin, but the squeezing is in a different direction. A cutoff frequency $k_c = 5$ was used to perform the tomographic process in all of them.	33
3.12 Wigner functions for the amplitude squeezed state reconstructed via quantum tomography over simulated quadrature marginal distributions using $\eta = \frac{\pi}{2}$. A cutoff frequency $k_c = 5$ was used.	34
3.13 Tomographic reconstruction for the vacuum state using two different values of k_c . In both cases, the result is not smooth.	34
3.14 Density matrices in the quadrature representation for the simulated vacuum state. p representation is portrayed on the left side and q on the right side.	35
3.15 Density matrices in the p representation (left) and q (right) representation for three different coherent states.	36
3.16 Density matrices in the quadrature representation, p in the left and q in the right, for the simulated thermal state.	37
3.17 Density matrices in the p representation (left) and q (right) representation for the squeezed vacuum.	38
3.18 Density matrix in the Fock representation for the simulated vacuum state.	39
3.19 Density matrices in the Fock representation for two different simulated squeezed vacuum states.	40
3.20 Density matrix in the number basis for the simulated thermal state.	40
3.21 Density matrix in the Fock representation for a simulated coherent state with $Re(\alpha) = Im(\alpha) = 3$	41
4.1 Schematic for the balanced homodyne detector. BS stands for beam splitter, L for lenses, PD for photodiode, and $\frac{\lambda}{2}$ for half wave plate. The doubled arrow specifies the movement of the piezo-electric.	43
4.2 Implementation of the homodyne detector according to Fig. 4.1. Half wave plates are not in position.	43

4.3 Subtractor using operational amplifiers. The schematic is on the left and the implementation using $3k\Omega$ resistors on the left.	44
4.4 Measurements for the outputs of the photodiodes and their subtraction for a fixed LO phase.	45
4.5 Averages of signals at both photodiodes and their subtraction for dif- ferent piezo-electric positions. The three amounts follow a sinusoidal shape.	45
4.6 Quadrature marginal distributions measured for a coherent state. (a) and (b) are the same graphic from different angles.	46
4.7 Wigner function reconstructed via quantum tomography for a co- herent state measured using balanced homodyne detection. Cutoff frequency $k_c = 2$ was used.	47
B.1 (a) quantum tomography GUI. (b) GUI while performing tomography.	64
B.2 Tomography results from two different perspectives as portrayed in the GUI.	65
B.3 Density matrices in the quadrature and Fock representation as shown in the GUI. Both results open in pop-up windows.	65
B.4 Set m and n values to calculate the density matrix on the Fock basis. .	65

Chapter 1

INTRODUCTION

Scientists, and physicists in particular, aim to understand and describe nature through experimentation, based on hypotheses derived from systematic observations and assumptions. This approach relies on the falsifiability of the hypotheses and the ability to reproduce experimental results. In this context, the conditions in which experiments are performed, the measurement instruments and the characteristics of the objects involved in it become a crucial factor to guarantee reproducibility.

In optics, light plays a fundamental role, as it is the goal of this field to understand the behavior and properties of such and its interaction with matter. Light as a physical object is a single entity. However, not all light is the same. It can vary in frequency, phase, and polarization among others. These differences are within the same physical object and they define the different states of light [1]. Knowing the state of light is equivalent to knowing all the characteristics that describe it, therefore characterizing it.

Measuring the state of light allows us to set initial conditions in an experiment and quantify changes during it. Therefore, achieving reproducibility in optics experiments will depend on how well the state of light is defined - or known-. The state of light also determines interactions with measurement instruments, as instrument outputs are dependent on light characteristics.

Measuring the state of light is a broad task considering light has multiple domains and characteristics [1]. In classical light, multiple measurements can be performed over the same state to obtain their characteristics. Nevertheless, quantum states are altered when measured, ergo the quantum nature of light makes it impossible to obtain its state by means of a single sample [2]. Although, obtaining the quantum state of light is feasible by measuring over multiple identically prepared samples [3].

Homodyne detection (HD) is a standard technique to obtain statistical information of light, therefore, yielding the opportunity to gain complete information over the state of light, even for short measurements. This method is widely used to perform time-domain [4] and frequency-domain [5] measurements and has allowed the

generation of interesting results such as the observation of squeezed states¹[\[5\]](#)[\[6\]](#). HD is also very useful for technologies that require well defined states. An example of this is satellite quantum key distribution based on coherent states, where HD is used for its efficiency and accuracy [\[7\]](#). The efficiency of this method has been demonstrated by the successful measurements perform over weak states [\[8\]](#). Alternative applications, such as random number generators [\[7\]](#)[\[9\]](#)[\[10\]](#), measuring the uncertainty relations of optical fields [\[8\]](#) and squeezed light sources characterization -useful for quantum-information processing [\[11\]](#) and gravitational wave detection[\[12\]](#)- have also been achieved using this technique.

In quantum mechanics, states are represented by a state vector and more generally by the density operator that describes the current state and how it will evolve given certain conditions [\[13\]](#). For quantum light, the properties of the density matrix can be encapsulated in a quasi-probability distribution that returns the probability of finding certain complex amplitudes [\[14\]](#). This function is known as the Wigner function and can be obtained from homodyne detection [\[3\]](#). This is achieved via quantum tomography [\[1\]](#). obtaining the Wigner function allows obtaining the density matrix [\[15\]](#) and therefore a full characterization of the quantum state of light.

This work aims to characterize a coherent state, a thermal state, a squeezed state, and the vacuum by the means of the reconstruction of the Wigner function through a tomography over the quadratures and the further calculation of the density matrix. The quadratures are simulated for each state and a first approach to homodyne detection on the frequency domain is taken by obtaining the quadratures for the coherent state via this method.

The (second) theory chapter of this work is written to give a comprehensive background about quantum states of light, homodyne detection: quadratures and the insights of this method, and quantum tomography: Radon inverse transform and numeric approximation. All the formalism required to understand this work is here.

The third chapter covers the reconstruction of the Wigner function for the states previously mentioned, the specificities about each one of them and the contrast with the theoretically expected functions. Afterward, the density matrix is obtained in two bases using the Wigner functions. All of this is done over simulated quadrature distributions.

After this, in the fourth chapter, the technical set up required to perform the

¹Squeezed light refers to light with reduced uncertainty in one of its components -quadratures-.

experimental measurements is explained. Due to the nature of the experimental technique, this chapter is divided into two main sections. The first one emphasizes in the optical set-up, while the second one does it on the electronic requirements - more specifically on the implementation of a signal subtractor-. Additional requirements, such as considering non-idealistic beam splitters [16], are also detailed in this chapter. Measurements are performed for the coherent state and the Wigner function is reconstructed using quantum tomography.

As a conclusion, the last chapter compiles all the results and work done in this thesis and yields the path for future applications.

Chapte r 2

THEORY

2.1 Quadrature representation

How do we represent light? First, we need to understand that light is a physical entity that we use to partially describe the reality that surrounds us. The objective is that this entity adjusts to what we observe in experiments and that all the properties we attribute to light are contained on it. Light behaves as a wave in certain situations and as a particle in others. Then, we can represent light as a particle or as a wave. But we must be careful, we want the representation of this object to follow the laws of physics as the real entity would. This will also depend on how we represent the environment around it and how we model interactions. The representation is chosen based on what's more convenient for visualizing or portraying certain physical phenomena, withholding all the characteristics mentioned before.

Quadrature representation is a way of representing light based on its complex amplitude [17]. This representation is useful as the quadratures are observables and they yield a phase space in which different states of light can be distinguished.

An approach to obtain this representation derives from rewriting the electric field of light. The electric field of light in time t with frequency ω is often expressed as

$$\vec{E}(\vec{r}, t) = \int \left[\mathcal{E}(\vec{k}, \omega) e^{i\vec{k}\cdot\vec{r}} e^{-i\omega t} + \mathcal{E}^*(\vec{k}, \omega) e^{-i\vec{k}\cdot\vec{r}} e^{i\omega t} \right] d^3\vec{k}\hat{e}, \quad (2.1)$$

where \mathcal{E} stands for the amplitude at a given point and \hat{e} for a particular polarization. Separating this expression into the transversely $\vec{q} = k_x\hat{x} + k_y\hat{y}$ and longitudinal $k_z\hat{z}$ terms in order that $\vec{k} = \vec{q} + k_z\hat{z}$, we obtain

$$\vec{E}(\vec{r}, t) = \int \mathcal{E}_q(\vec{q}) \mathcal{E}_{k_z}(k_z) \mathcal{E}_\omega(\omega) e^{i\vec{q}\cdot\vec{r}} e^{ik_z z} e^{-i\omega t} d^2\vec{q} dk_z \hat{e} + CC, \quad (2.2)$$

in which CC is the complex conjugate. As the electric field will be predominant in one direction, the paraxial approximation is used $\frac{\omega}{c} = |\vec{k}| \approx k_z$. Defining $\mathcal{E}_{\tilde{\omega}}(\tilde{\omega}) = \mathcal{E}_{k_z}(k_z)\mathcal{E}_\omega(\omega)$ and $t' = z/c$, yields

$$\vec{E}(\vec{r}, t) = \int \mathcal{E}_q(\vec{q}) \mathcal{E}_{k_z}(k_z) \mathcal{E}_\omega(\omega) e^{i\vec{q}\cdot\vec{p}} e^{ik_z z} e^{-i\omega t} \frac{d^2\vec{\rho} d\omega}{c} \hat{e} + CC \quad (2.3)$$

$$\approx \int \mathcal{E}_q(\vec{q}) \mathcal{E}_{\tilde{\omega}}(\tilde{\omega}) e^{i\vec{q}\cdot\vec{p}} e^{-i\tilde{\omega}(t-t')} d^2\vec{\rho} d\tilde{\omega} \hat{e} + CC \quad (2.4)$$

$$\approx \int \mathcal{E}_q(\vec{q}) e^{i\vec{q}\cdot\vec{p}} d^2\vec{\rho} \hat{e} \int \mathcal{E}_{\tilde{\omega}}(\tilde{\omega}) e^{-i\tilde{\omega}(t-t')} d\tilde{\omega} \hat{e} + CC. \quad (2.5)$$

Dropping the transverse expression, a single mode of the electric field in the temporal component is expressed as

$$E(z, t) = \mathcal{E}_{\tilde{\omega}}(\tilde{\omega}) e^{-i\tilde{\omega}(t-t')} + \mathcal{E}_{\tilde{\omega}}^*(\tilde{\omega}) e^{i\tilde{\omega}(t-t')} \quad (2.6)$$

$$= \alpha(\tilde{\omega}) e^{-i\tilde{\omega}t} + \alpha^*(\tilde{\omega}) e^{i\tilde{\omega}t} \quad (2.7)$$

$$= \alpha(\tilde{\omega}) [\cos(\tilde{\omega}t) - i \sin(\tilde{\omega}t)] + \alpha^*(\tilde{\omega}) [\cos(\tilde{\omega}t) + i \sin(\tilde{\omega}t)] \quad (2.8)$$

$$= \underbrace{[\alpha(\tilde{\omega}) + \alpha^*(\tilde{\omega})] \cos(\tilde{\omega}t)}_{X_1(\tilde{\omega})} + i \underbrace{[-\alpha(\tilde{\omega}) + \alpha^*(\tilde{\omega})] \sin(\tilde{\omega}t)}_{X_2(\tilde{\omega})}, \quad (2.9)$$

here $\alpha = \mathcal{E}_{\tilde{\omega}}(\tilde{\omega}) e^{ik_z z}$. X_1 and X_2 are known as *quadratures* as there is a 90° phase difference between them. Quadratures represent the real and imaginary amplitude of the light field as shown in equation (2.9) and they fully describe the optical field.

Quadratures can be conveniently drawn in a *phasor diagram*. Phasor diagrams are commonly used in electronic engineering to compare sinusoidal signals of the same frequency. As the name suggests, it especially useful to perceive phase differences. In quadratures, this phase difference accounts for where $t = 0$, so a ϕ phase can be introduced into equation (2.9) yielding

$$E(z, t) = X(\phi) \cos(\omega t + \phi) + iX\left(\phi + \frac{\pi}{2}\right) \sin(\omega t + \phi), \quad (2.10)$$

where $X(\phi) = X_1(\omega)e^{i\phi}$. Phase ϕ will always need to be related to a reference, as it has no meaning without it. Note that phase ϕ is already in Eq. (2.9). In general $\alpha(r, t) = \alpha_0(r, t)e^{i\phi(r,t)}$ [17] and for a monochromatic plane wave in equation (2.9) $\phi(z) = k_z \cdot z$.

Figure 2.1 represents the phasor diagram for an electric field with phase ϕ and magnitude \mathcal{E}_0 . Although it may seem completely accurate, it is not for a quantized light field as the uncertainty has not yet been taken into account. Furthermore, the

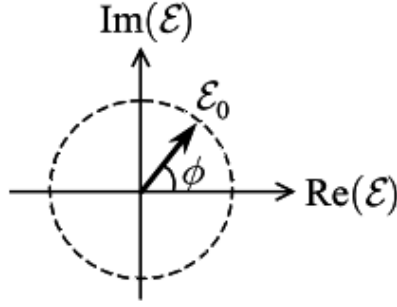


Figure 2.1: The phasor diagram for an electric field with phase ϕ and magnitude E_0 [2].

phasor diagram can also be interpreted in terms of photon number as $E_0 = |\mathcal{E}| = \sqrt{\bar{n}}$ where \bar{n} is the average photon number [2].

From a quantum perspective, quadratures can be defined as operators [1]

$$\hat{q} = \frac{1}{\sqrt{2}} (\hat{a}^\dagger + \hat{a}), \quad \hat{p} = \frac{i}{\sqrt{2}} (\hat{a}^\dagger - \hat{a}). \quad (2.11)$$

These definitions are conceived such that [1]

$$\hat{a} = \frac{1}{\sqrt{2}} (\hat{q} + i\hat{p}), \quad (2.12)$$

making \hat{q} and \hat{p} be the real and imaginary component of the electric field amplitude. The eigenstates $|q\rangle$ and $|p\rangle$ are orthogonal and complete. However, they are not a basis in the sense of Hilbert as they are not truly normalizable [13]. In quantum optics quadratures are considered momentum and position like amounts due to the similarity in between the commutators for these two quantities, $[\hat{q}, \hat{p}] = [\hat{x}, \hat{p}] = i$ in natural units. Although this similarity, quadratures are not momentum and position, they are components of the electric field amplitude. As one would expect for a quantity kindred to position and momentum, there is a relation between these states through a Fourier transform [1]

$$|q\rangle = \frac{1}{\sqrt{2\pi}} \int_{-\infty}^{\infty} e^{-iqp} |p\rangle \quad |p\rangle = \frac{1}{\sqrt{2\pi}} \int_{-\infty}^{\infty} e^{iqp} |q\rangle. \quad (2.13)$$

According to the commutation relationship of \hat{q} and \hat{p} , the minimum uncertainty principle applies as they do not commute. The minimum uncertainty can be easily calculated using the relation to the commutator, in general

$$\Delta \hat{A}^2 \Delta \hat{B}^2 \geq \left| \frac{1}{2i} \langle [\hat{A}, \hat{B}] \rangle \right|^2, \quad (2.14)$$

for any observables \hat{A} and \hat{B} , where $\Delta\hat{A}$ and $\Delta\hat{B}$ are standard deviations [18]. Applying Eq. (2.14) to \hat{q} and \hat{p} we get

$$\Delta\hat{q}^2\Delta\hat{p}^2 \geq \left| \frac{1}{2i} \langle [\hat{q}, \hat{p}] \rangle \right|^2 \quad (2.15)$$

$$\Delta\hat{q}^2\Delta\hat{p}^2 \geq \left| \frac{1}{2i} \langle i \rangle \right|^2 \quad (2.16)$$

$$\Delta\hat{q}^2\Delta\hat{p}^2 \geq \frac{1}{4}. \quad (2.17)$$

The result on equation 2.17 leads to consider a phasor diagram as the one in figure 2.2 for quantized light fields, where uncertainty is considered. Therefore, instead of a dot, the phasor tip is a circle. It is important to note that the value encounter on equation 2.17 can scale to arbitrary values during experimental procedures [19].

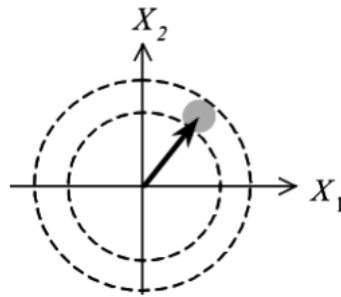


Figure 2.2: Phasor diagram for quadratures X_1 and X_2 considering their uncertainty [2].

2.2 Balanced homodyne detection

Although quadrature representation is useful to compare different light fields and easily visualize their phase and amplitude properties, its main attraction comes from the fact that quadratures can be measured experimentally. Thus, in some sense, it can be considered as a primary representation that should have appeared naturally.

The most straightforward way of characterizing a light source is photon counting. In this way, different states of light can be detected and classified, but it is difficult to accurately measure high power sources, as detectors can not measure fast enough to account for individual photons [2]. Therefore photodiodes are used.

Photodiodes are devices that deliver a current proportional to the power of the beam that incides on them. They are also frequency dependant and proportional

to an efficiency η . Statistical properties of light can be gain using photodiodes by measuring fluctuations on the currents they generate as they account for photon number fluctuations. Intensity fluctuations can also be due to other factors such as mechanical vibrations in the cavity mirrors of lasers and other classical noise sources [2], hence to better obtain statistical light properties it is important to reduce noise not accounted for photon number fluctuations.

Balanced homodyne detection is one method to obtain quadratures from a light field directly. This method relays on the comparison of the light source to be characterized and a reference source. Photodiodes are used as detectors. It was introduced in the early eighties [20] as a step forward in balanced detection and demonstrated to reduce correlated (classical) noise [21]. Phase information is also available when this technique is used and it can be obtained in comparison to the reference field.

The main schematic for a balanced homodyne detector is presented in figure 2.3. It consists of a beam-splitter (BS) and two photo-detectors (P_1 and P_2). The reference signal or local oscillator LO, and the light source that is going to be characterized (S) are optically mixed in the BS and then detected. The detected currents are then subtracted, this subtraction eliminates classical fluctuations as they are correlated in both outputs of the beam-splitter [2].

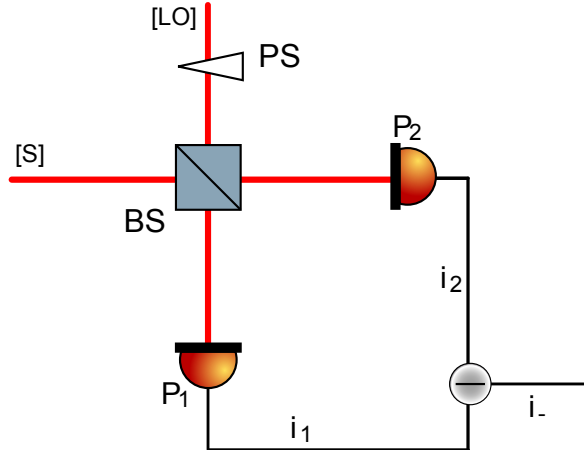


Figure 2.3: Schematic for homodyne detection. LO is the local oscillator and S the field that is going to be characterized. PS allows phase shifting in the LO and the subtracted current i_- yields the quadratures of S.

The light fields at the BS outputs are described by the reflected and transmitted components of the input light. For general inputs, In_1 and In_2 with phase zero,

$\phi_{In_1} = \phi_{In_2} = 0$, the BS outputs are described as [17]

$$\mathcal{E}_{Out_1} = \sqrt{(1-\epsilon)}\mathcal{E}_{In_1}e^{i\phi_{In_1t}} + \sqrt{\epsilon}\mathcal{E}_{In_2}e^{i\phi_{In_2t}} \quad (2.18)$$

$$\mathcal{E}_{Out_2} = \sqrt{\epsilon}\mathcal{E}_{In_1}e^{i\phi_{In_1r}} + \sqrt{(1-\epsilon)}\mathcal{E}_{In_2}e^{i\phi_{In_2r}}, \quad (2.19)$$

where ϵ corresponds to the BS efficiency. As this is balanced detection, the BS is 50/50 and $\epsilon = \frac{1}{2}$. The transmitted and reflected relative phases also have to be determined. Applying energy conservation, [17]

$$|\mathcal{E}_{In_1}|^2 + |\mathcal{E}_{In_2}|^2 = |\mathcal{E}_{Out_1}|^2 + |\mathcal{E}_{Out_2}|^2 \quad (2.20)$$

$$\begin{aligned} |\mathcal{E}_{In_1}|^2 + |\mathcal{E}_{In_2}|^2 &= |\mathcal{E}_{In_1}|^2 + |\mathcal{E}_{In_2}|^2 \\ &+ \sqrt{\frac{1}{4}} \left(\mathcal{E}_{In_2}^* \mathcal{E}_{In_1} e^{i(\phi_{In_1t} - \phi_{In_2t})} + CC \right. \\ &\left. + \mathcal{E}_{In_1} \mathcal{E}_{In_2}^* e^{i(\phi_{In_1r} - \phi_{In_2r})} + CC \right). \end{aligned} \quad (2.21)$$

The last term in Eq.(2.21) must be zero in order to keep the equality true. Therefore,

$$\begin{aligned} 0 &= \mathcal{E}_{In_1} \mathcal{E}_{In_2}^* \left(e^{i(\phi_{In_1t} - \phi_{In_2t})} + e^{i(\phi_{In_1r} - \phi_{In_2r})} \right) \\ &+ \mathcal{E}_{In_1}^* \mathcal{E}_{In_2} \left(e^{-i(\phi_{In_1t} - \phi_{In_2t})} + e^{-i(\phi_{In_1r} - \phi_{In_2r})} \right). \end{aligned} \quad (2.22)$$

It can be demonstrated that Eq.2.22 is zero when

$$0 = e^{i(\phi_{In_1t} - \phi_{In_2t})} + e^{i(\phi_{In_1r} - \phi_{In_2r})}. \quad (2.23)$$

All of the relative phases can be set to zero but ϕ_{In_2r} that is set to π , resulting in a phase shift of 180° in the reflected beam of one the inputs [17]. This solution satisfies equation (2.23) and simplifies equations (2.18) and (2.19) into

$$\mathcal{E}_{Out_1} = \frac{1}{\sqrt{2}}\mathcal{E}_{In_1} + \frac{1}{\sqrt{2}}\mathcal{E}_{In_2} \quad (2.24)$$

$$\mathcal{E}_{Out_2} = \frac{1}{\sqrt{2}}\mathcal{E}_{In_1} - \frac{1}{\sqrt{2}}\mathcal{E}_{In_2}. \quad (2.25)$$

Using these results, we introduce the LO and S as inputs and keep a relative phase difference between them, so that ϕ_{LO} appears

$$\mathcal{E}_{P1} = \frac{1}{\sqrt{2}}\mathcal{E}_{LO}e^{i\phi_{LO}} + \frac{1}{\sqrt{2}}\mathcal{E}_S \quad (2.26)$$

$$\mathcal{E}_{P2} = \frac{1}{\sqrt{2}}\mathcal{E}_{LO}e^{i\phi_{LO}} - \frac{1}{\sqrt{2}}\mathcal{E}_S. \quad (2.27)$$

The \mathcal{E}_S field amplitude can be expressed as quadratures, as this representation is general. The LO is continue to be treated as it was

$$\mathcal{E}_{P_1} = \frac{1}{\sqrt{2}} \mathcal{E}_{LO} e^{i\phi_{LO}} + \frac{1}{\sqrt{2}} (X_{1_{\mathcal{E}_S}} + iX_{2_{\mathcal{E}_S}}) \quad (2.28)$$

$$\mathcal{E}_{P_2} = \frac{1}{\sqrt{2}} \mathcal{E}_{LO} e^{i\phi_{LO}} - \frac{1}{\sqrt{2}} (X_{1_{\mathcal{E}_S}} + iX_{2_{\mathcal{E}_S}}) \quad (2.29)$$

$$\mathcal{E}_{P_1} = \frac{1}{\sqrt{2}} \left[(\mathcal{E}_{LO} \cos(\phi_{LO}) + X_{1_{\mathcal{E}_S}}) + i(\mathcal{E}_{LO} \sin(\phi_{LO}) + X_{2_{\mathcal{E}_S}}) \right] \quad (2.30)$$

$$\mathcal{E}_{P_2} = \frac{1}{\sqrt{2}} \left[(\mathcal{E}_{LO} \cos(\phi_{LO}) - X_{1_{\mathcal{E}_S}}) + i(\mathcal{E}_{LO} \sin(\phi_{LO}) - X_{2_{\mathcal{E}_S}}) \right]. \quad (2.31)$$

The current at the detectors would be proportional to the intensity at each detector, then the subtraction of this currents is [2]

$$i_1 - i_2 \propto |\mathcal{E}_{P_1}|^2 - |\mathcal{E}_{P_2}|^2 \quad (2.32)$$

$$\propto \mathcal{E}_{P_1} \mathcal{E}_{P_1}^* - \mathcal{E}_{P_2} \mathcal{E}_{P_2}^*. \quad (2.33)$$

Inserting expressions in Eq. (2.30) and Eq. (2.31) into Eq. (2.33), the current subtraction is

$$\begin{aligned} i_1 - i_2 &\propto \frac{1}{2} \left[(\mathcal{E}_{LO} \cos(\phi_{LO}) + X_{1_{\mathcal{E}_S}})^2 + (\mathcal{E}_{LO} \sin(\phi_{LO}) + X_{2_{\mathcal{E}_S}})^2 \right] \\ &\quad - \frac{1}{2} \left[(\mathcal{E}_{LO} \cos(\phi_{LO}) - X_{1_{\mathcal{E}_S}})^2 + (\mathcal{E}_{LO} \sin(\phi_{LO}) - X_{2_{\mathcal{E}_S}})^2 \right] \end{aligned} \quad (2.34)$$

$$\begin{aligned} i_1 - i_2 &\propto \frac{1}{2} \left[2\mathcal{E}_{LO} \cos(\phi_{LO}) X_{1_{\mathcal{E}_S}} + 2\mathcal{E}_{LO} \sin(\phi_{LO}) X_{2_{\mathcal{E}_S}} \right. \\ &\quad \left. + 2\mathcal{E}_{LO} \cos(\phi_{LO}) X_{1_{\mathcal{E}_S}} + 2\mathcal{E}_{LO} \sin(\phi_{LO}) X_{2_{\mathcal{E}_S}} \right] \end{aligned} \quad (2.35)$$

$$i_1 - i_2 \propto 2\mathcal{E}_{LO} \left[\cos(\phi_{LO}) X_{1_{\mathcal{E}_S}} + \sin(\phi_{LO}) X_{2_{\mathcal{E}_S}} \right]. \quad (2.36)$$

In a real experiment, detectors measure currents i_1 and i_2 as an average in time due to its finite response time. Therefore Eq. (2.36) becomes

$$\langle i_1 - i_2 \rangle_t \propto 2 \langle \mathcal{E}_{LO} \rangle_t \left[\cos(\phi_{LO}) \langle X_{1_{\mathcal{E}_S}} \rangle_t + \sin(\phi_{LO}) \langle X_{2_{\mathcal{E}_S}} \rangle_t \right]. \quad (2.37)$$

The result in Eq. (2.37) shows that the subtracted current allows the measurement of the quadratures of S. This is achieved by changing the phase of the local oscillator. For $\phi_{LO} = n\pi \ \forall n \in \mathbb{N}$ the value of $X_{1_{\mathcal{E}_S}}$ is obtained, for $\phi_{LO} = n\pi + \frac{\pi}{2} \ \forall n \in \mathbb{N}$ the value of $X_{2_{\mathcal{E}_S}}$ and for any other value of ϕ_{LO} a combination of both quadratures is

obtained. The phase shifter in figure 2.3 is used for this purpose. By performing multiple measurements for the same phase, the probability distribution for the given quadrature is obtained.

Balanced homodyne detection can also be approached from a more quantum perspective. Taking two modes as inputs, a and b , such that a represents the LO and b represents S, the process to obtain the quadratures from the subtracted current can be repeated. As the LO is a laser it can be written as a coherent state $|\alpha\rangle = |\alpha_{LO}|e^{-i(\omega t+\psi)}$ (see section 2.3), to simplify further calculation ψ is set to $\psi = \phi + \frac{\pi}{2}$. Homodyne detection relays on S having the same frequency as the LO, in contrast to heterodyne detection in which the frequencies are different. Taking this into account, \hat{b} can be separated into amplitude and a frequency $\hat{b} = \hat{b}_0 e^{-i\omega t}$. The BS operators relationships are [22]

$$\hat{c} = \frac{1}{\sqrt{2}} (\hat{a} + i\hat{b}) \quad (2.38)$$

$$\hat{d} = \frac{1}{\sqrt{2}} (i\hat{a} + \hat{b}), \quad (2.39)$$

for inputs a and b and outputs c and d . The subtracted current will then be [22]

$$\langle i_1 - i_2 \rangle_t = \langle \hat{c}^\dagger \hat{c} - \hat{d}^\dagger \hat{d} \rangle_t \quad (2.40)$$

$$= i \langle \hat{a}^\dagger \hat{b} - \hat{a} \hat{b}^\dagger \rangle_t \quad (2.41)$$

$$= \langle |\alpha_{LO}|e^{i(\omega t+\phi)}\hat{b} + |\alpha_{LO}|e^{-i(\omega t+\phi)}\hat{b}^\dagger \rangle_t \quad (2.42)$$

$$= |\alpha_{LO}| \langle e^{i(\omega t+\phi)}\hat{b}_0 e^{-i\omega t} + e^{-i(\omega t+\phi)}\hat{b}_0^\dagger e^{i\omega t} \rangle_t \quad (2.43)$$

$$= |\alpha_{LO}| \langle \hat{b}_0 e^{i\phi} + \hat{b}_0^\dagger e^{-i\phi} \rangle_t \quad (2.44)$$

$$= \sqrt{2} |\alpha_{LO}| \langle \hat{X}(\phi) \rangle_t, \quad (2.45)$$

were $\hat{X}(\phi) = \frac{1}{\sqrt{2}} (\hat{b}_0 e^{i\phi} + \hat{b}_0^\dagger e^{-i\phi})$. $\hat{X}(\phi)$ is known as the generalized field quadrature operator [22] as it yields the quadratures from Eq. (2.11) when the LO phase is $\phi = 0$ or $\phi = -\frac{\pi}{2}$.

From equations (2.37) and (2.45) it is clear that balanced homodyne detection is suited for quadrature detection by means of changing the phase of the LO. This detector also cancels out correlated fluctuations, allowing better performance.

2.3 Quantum states of light

States of light are optical fields that withhold certain properties that are of physical or mathematical interest. Such properties include very well-defined number of

photons or high coherence (ability to interfere in the time or spatial domain [23]). All of them have characteristics that allow them to be identified as part of a main state but also include characteristics that permit them to vary in between their own state. Defining these states is useful, not only because they are states of the electromagnetic oscillator, but because they are real observable states of light that will behave in particular ways [1].

Density operator and its matrix representation

Quantum mechanics are based on the probability of systems being on a determined state at a given time and their evolution. This states can be the superposition or a statistical mixture of other states on a given basis. Superpositions or pure states can easily be represented by linear combinations of other pure states $|\psi_k\rangle$, while statistical mixtures can not be represented in this way as they are probabilistic. The density operator for a pure state $\hat{\rho} = |\psi_k\rangle\langle\psi_k|$ and the density operator for a statistical mixture $\hat{\rho} = \sum_k p_k |\psi_k\rangle\langle\psi_k|$ are introduced to obtain the coefficients of the linear combinations yielded by pure states and the probabilities yielded by statistical mixtures p_k . This operator can be enclosed by a basis, generating the density matrix $\rho_{nm} = \langle u_n | \hat{\rho} | u_m \rangle$. The density matrix is a powerful tool that encapsulates the statistical information of the state on a given basis [13].

The density matrix in the quadrature representation is defined as

$$\rho_{qp} = \langle q | \hat{\rho} | p \rangle, \quad (2.46)$$

for $\hat{q} |q\rangle = q |q\rangle$ and $\hat{p} |p\rangle = p |p\rangle$. Another particular representation is useful in optics, it is the Fock representation. It is defined from the photon number operator $\hat{n} = \hat{a}^\dagger \hat{a}$ and represents the number of photons of a given state. The density matrix on this state is

$$\rho_{nm} = \langle n | \hat{\rho} | m \rangle, \quad (2.47)$$

where $\hat{n} |n\rangle = n |n\rangle$ and $\hat{n} |m\rangle = m |m\rangle$.

Coherent states

Coherent states were introduced as minimum uncertainty states inspired on the wave packets of the harmonic oscillator [24]. They are eigenstates of the annihilation operator and are coherent, as their phase difference is constant, so they can interfere in time or in space [23]; actually they are highly coherent as their degree of coherence is always one. Their amplitude and phase are very well defined and Lasers are the

most common source of this type of light. A coherent state is written as $|\alpha\rangle$ where

$$\hat{a}|\alpha\rangle = \alpha|\alpha\rangle, \quad (2.48)$$

note that α is a complex amplitude as the annihilation operator is not an observable. It can be decomposed into quadratures and represented in the phasor diagram using Eq. (2.12). The coherent state representation in the phasor diagram is naturally a circle displaced from the center by the state amplitude magnitude $|\alpha|$. The diameter of this circle corresponds to the minimum uncertainty for each quadrature for the coherent states, which is $\frac{1}{2}$ according to equation (2.17). Figure 2.4 depicts this phasor diagram.

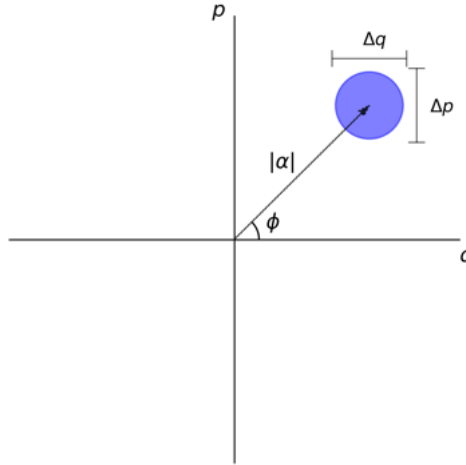


Figure 2.4: Phasor diagram for a coherent state with amplitude α and phase ϕ . $\Delta q = \Delta p$ and follow the relation on Eq. 2.17

On the Fock representation, the coherent states are [25]

$$|\alpha\rangle = e^{-\frac{1}{2}|\alpha|^2} \sum_{n=0}^{\infty} \frac{\alpha^n}{\sqrt{n!}} |n\rangle. \quad (2.49)$$

From this expression and using the definition in Eq. (2.47) the density matrix in the Fock basis for a coherent state can be calculated to be

$$\rho_{nm} = \frac{e^{-|\alpha|^2} \alpha^n \alpha^{*m}}{\sqrt{n!m!}}. \quad (2.50)$$

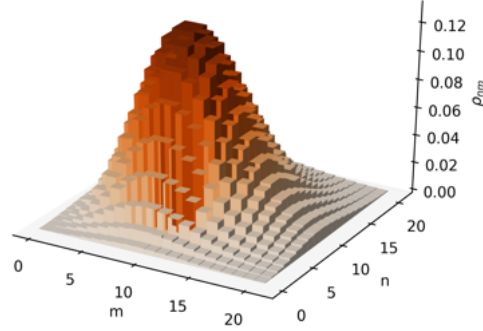


Figure 2.5: Density matrix ρ_{nm} for a coherent state with an amplitude $\alpha = 3$.

Thermal states

Thermal states are regarded as states in thermal equilibrium. This equilibrium is due to interactions with matter or because it is emitted by black body radiation [24]. They are the most common type of light: natural light, and unlike coherent states, its amplitude is not very well defined, but on average is zero. Thermal states can be expressed as a statistical mixture of number states and follow thermodynamics rules, thus its name. The probability of having n number of photons in one mode of this state is given by Bose–Einstein distribution [2]. This leads to a density operator [24]

$$\hat{\rho} = (1 - \beta) \sum_{n=0}^{\infty} e^{-n\beta} |n\rangle \langle n|, \quad (2.51)$$

where $\beta = \frac{\hbar\omega}{K_B T}$. This equation yields a diagonal density matrix,

$$\rho_{nn} = (1 - \beta)e^{-n\beta}. \quad (2.52)$$

This matrix is shown in figure 2.7, according to Eq. (2.52). In the phasor diagram its a figure of non-minimum uncertainty that changes amplitude and phase as they are not very well defined, but on average stays at zero amplitude.

Vacuum

The vacuum state is a particular case of the coherent states where the amplitude $\alpha = 0$. The $|\alpha = 0\rangle$ state is considered the vacuum state as it has zero amplitude on average and it is present in the absolute vacuum, this can be shown by the Casimir force [2]. Although on average it is a zero-point amplitude, it fluctuates due to the

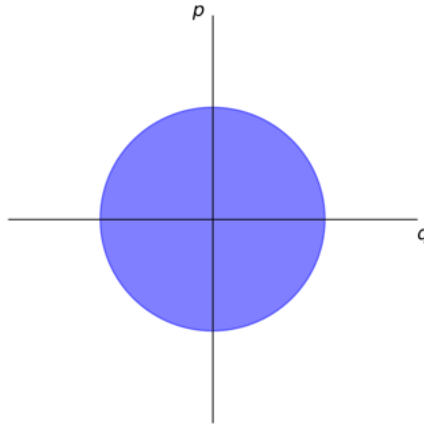


Figure 2.6: Phasor diagram for a thermal state. This state is centered in zero, as on average it has no amplitude, and uncertainty on both quadratures is equal. It is not a minimum uncertainty state

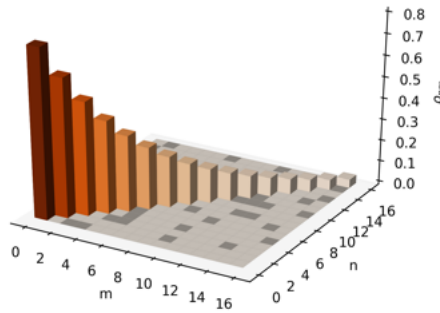


Figure 2.7: Density matrix ρ_{nm} for a thermal state with $\beta = 0.2$. This matrix is a statistical mixture, therefore the matrix is diagonal.

uncertainty principle. The phasor diagram (Fig. 2.8) representing this state reflects this and would be the same as a coherent state, but with no amplitude in any axis, just the minimum uncertainty. This state can be detected using homodyne detection by leaving the S input empty [2]. As a coherent state, the vacuum state follows Eq. (2.50), therefore its density matrix is similar to the one of the coherent state but centered at zero (Fig. 2.9).

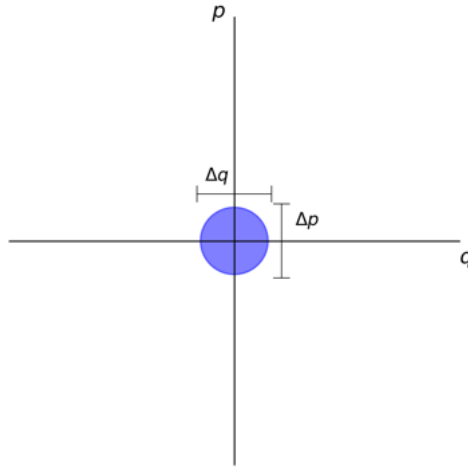


Figure 2.8: Phasor diagram for the vacuum state. As expected it is centered at the origin zero, as on average it has no amplitude. As a minimum-uncertainty state Δp and Δq follow the relation on Eq. (2.17)

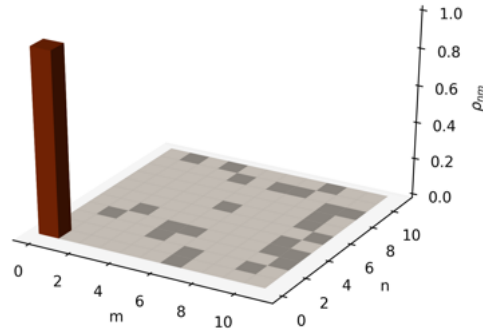


Figure 2.9: Density matrix ρ_{nm} for the vacuum state according to Eq. (2.50) using $\alpha = 0$. The vacuum state is a state with zero photons.

Squeezed states

Squeezed states are states that have different uncertainties in each quadrature, leading to squeezed circle, ellipse, in the phasor diagram [2]. By their nature, they are purely quantum states and can not be differentiated from other states via classic measurements. The squeezing can be in any direction. A particular squeezed state is the squeezed vacuum. This state has amplitude $\alpha = 0$ and minimum uncertainty as

the vacuum state, but the uncertainty is not equally distributed on both quadratures. It was first observed in the mid-eighties using homodyne detection with uncertainties on a given quadrature that were smaller than the one for the vacuum states [5]. Other types of squeezed states are the coherent squeezed states. These states have an amplitude α as a coherent state, but again their uncertainty relationship is not equally distributed. However, they continue minimum uncertainty states. The phasor diagrams for the squeezed vacuum, amplitude squeezed coherent and phase squeezed coherent states are depicted in Fig (2.10). The last two states are known this way because the first one is elongated in the ϕ direction while the second one's uncertainty is bigger in the radial direction, where the amplitude α is represented.

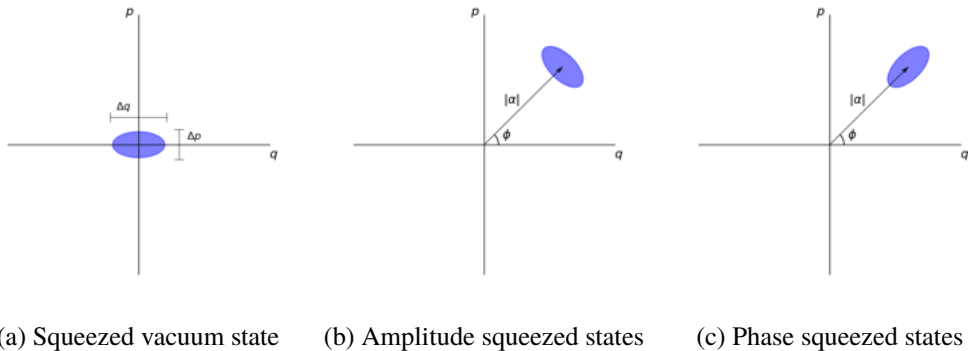


Figure 2.10: Phasor diagram for the vacuum squeezed state (a), phase squeezed states (b) and amplitude squeezed states (c). The uncertainty relationship for these states complies with the uncertainty principle in Eq. (2.17), but is not evenly distributed.

The squeezed states can be described by three parameters: the squeezing parameter ξ that represents how much the state is squeezed, an angle θ that allows the squeezing to be rotated and, an amplitude α . In general, a squeezed state on the Fock representation can be written as [22]

$$|\alpha, \xi\rangle = \frac{1}{\sqrt{\cosh(r)}} e^{-\frac{1}{2}|\alpha|^2 - \frac{1}{2}\alpha^{*2} e^{i\theta} \tanh(r)} \times \sum_{n=0}^{\infty} \frac{(e^{i\theta} \tanh(r))^{\frac{n}{2}}}{\sqrt{n!}} H_n \left(\frac{\gamma}{e^{i\theta} \sinh(2r)} \right) |n\rangle, \quad (2.53)$$

where r accounts for the squeezing factor, H_n for the Hermite polynomials of degree n and $\gamma = \alpha \cosh(r) + \alpha^* e^{i\phi} \sinh(r)$. The squeezed vacuum can be written in a much simpler expression [22]

$$|\xi\rangle = \frac{1}{\sqrt{\cosh(r)}} \sum_{m=0}^{\infty} (-1)^m \frac{(2m)!}{2^m m!} e^{im\theta} \tanh(r)^m |2m\rangle. \quad (2.54)$$

From this expression, the density matrix is calculated to be

$$\rho_{nm} = \frac{1}{\cosh(r)} (-1)^{m+n} \frac{(2m)!(2n)!}{2^m m! 2^n n!} e^{i(m-n)\theta} \tanh(r)^{m+n}, \quad (2.55)$$

for even values of n and m . This implies that the density matrix in the Fock representation for the squeezed vacuum only has values different from zero in even values of n and m , as shown in Fig. (2.11).

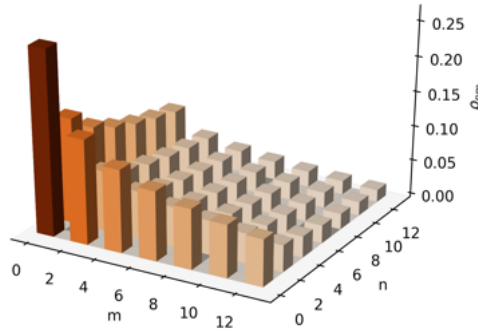


Figure 2.11: Density matrix ρ_{nm} for the squeezed vacuum state with a squeezing factor of 2 and $\theta = 0$. This matrix only has non zero values on even values of n and m .

2.4 Wigner function

The density matrix described in section 2.3 was a way of describing states in terms of statistical information. Moreover, another approach can be taken into describing states, distribution functions [26]. The quantum nature of the states of light that are going to be described, binds them to the uncertainty principle, which implies that the phase space probability distribution of a state on quadrature q and p is not very well defined as simultaneous measurements can not be performed [14]. Then quasi-probability distribution functions are defined to overcome this impediment. They are quasi in the sense that they can encounter negative values. The first and most famous of these distributions is the Wigner distribution, introduced in the early thirties [27]. Quasi-probability distribution functions are useful as calculation tools and because they depict quantum properties [14].

The Wigner function for quadratures is defined as [14][27]

$$W(q, p) = \frac{1}{2\pi} \int_{-\infty}^{+\infty} e^{ipx} \langle q - x/2 | \hat{\rho} | q + x/2 \rangle dx. \quad (2.56)$$

In this way the one to one relation between the Wigner function and the density matrix is clear but is not as useful for the purpose of this work. Instead, the Wigner function is going to be approached only by assuming it behaves like a joint probability [1] so that it can be related to the distributions of quadratures. The approach to derive the function by stating its properties was developed in the late eighties [28]. As a joint probability distribution, the marginal distributions of $W(q, p)$ should yield q and p . In this sense the marginal distribution for q after a phase shift ϕ can be defined as [1]

$$\begin{aligned} pr(q, \phi) &:= \langle q | \hat{U}(\theta) \hat{\rho} \hat{U}^\dagger(\theta) | q \rangle \\ &= \int_{-\infty}^{+\infty} W(q \cos(\theta) - p \sin(\theta), p \cos(\theta) + q \sin(\theta)) dp, \end{aligned} \quad (2.57)$$

where $\hat{U}(\phi) = e^{-i\phi\hat{n}}$ is the phase-shifting operator. When Eq. (2.57) is evaluated for $\phi = 0$ and $\phi = \frac{\pi}{2}$ it yields the partial distributions for q and p ($\hat{U}^\dagger(\frac{\pi}{2})|q\rangle$ is an eigenstate $|p\rangle$) and it fulfills the condition of being a joint probability [1]. The original definition of the Wigner function as it is in Eq. (2.56) can be recovered from Eq. (2.57) by performing a Fourier transform and expanding the operators' definitions, the full process can be found in [1].

The Wigner function can be analytically calculated if the density matrix is known according to Eq. (2.56), it can also be obtained via quantum tomography using quadrature distributions (see section 2.5). The Wigner function is similar in shape to the phasor diagram as both represent quadrature values, but the Wigner function adds a sense of probability. The Wigner functions for the coherent, vacuum, thermal, and squeezed states are depicted in figure 2.12 and as expected $W(q, p)$ for the coherent is a gaussian shaped mountain from a distance α from the origin. The Wigner function for the vacuum is very similar to the one of the coherent state but center in the origin. This makes sense as a projection from above will turn into the phasor diagram [17]. $W(q, p)$ for the squeezed state is a long shaped gaussian that reflects the squeezing quadrature. Finally, the thermal state is represented by a low hill as nor phase or amplitude is well defined.

Analytically the Wigner function for the vacuum, coherent, squeezed, and thermal states described in section 2.3 can be calculated using Eq. (2.56) and the density matrices of each state [1].

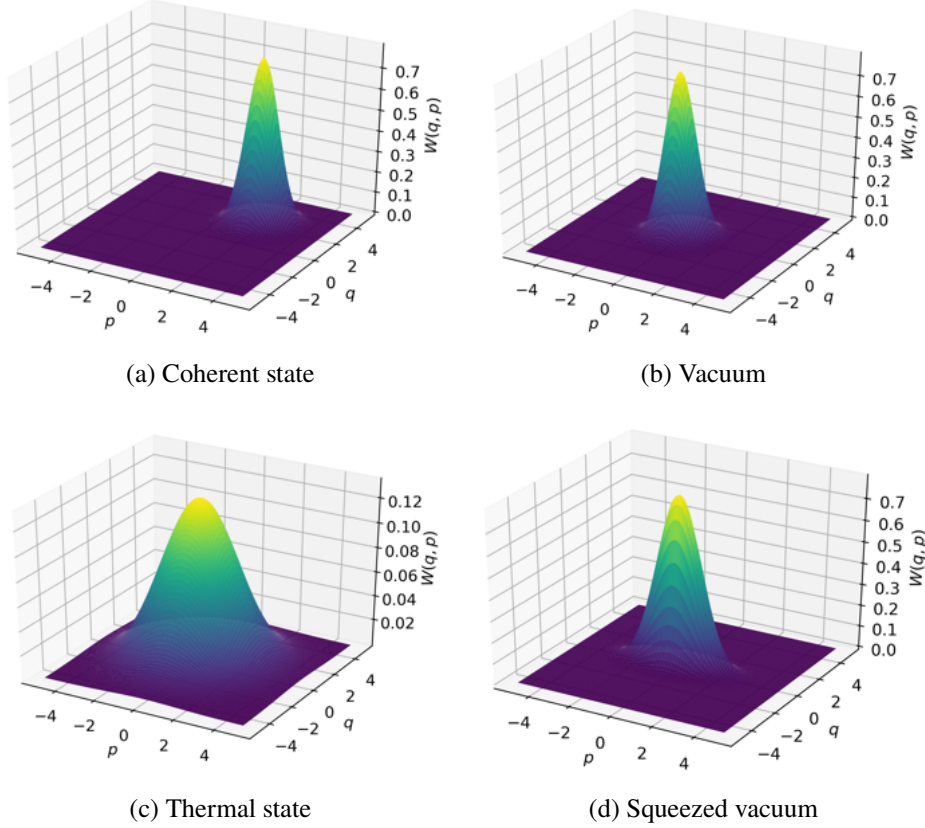


Figure 2.12: Wigner functions for multiple states obtained using the analytical solution.

2.5 Quantum tomography

Radon inverse transform

Quantum tomography aims to reconstruct the Wigner function from the partial distributions of quadratures, usually coming from homodyne detection. It was first performed in the early nighties for quantum states [29] based on the work on [30]. It has even been used to reconstruct the Wigner functions for states that are a combination of other states [31]. The whole process is based on what is known as the Radon inverse transform. The expression in Eq. (2.57) is in the form of a Radon integral and therefore its inverse can be found using the Radon inverse transform [32]. The Radon inverse transform allows to reconstruct an object from its projections, in this case, the quadrature amplitudes for a given phase ϕ .

From Eq. (2.57) an expression for the Wigner function in terms of the quadrature distributions can be obtained using its Fourier transform. The Fourier transform of

the Wigner function is known as the characteristic function [1]

$$\tilde{W}(u, v) = \int_{-\infty}^{+\infty} \int_{-\infty}^{+\infty} W(q, p) e^{-i(uq+vp)} dq dp, \quad (2.58)$$

and the Wigner function is recovered from it using the inverse Fourier transform. Now we can also take the Fourier transform of the quadrature distributions in Eq. (2.57) [1]

$$\begin{aligned} \tilde{pr}(\xi, \phi) &= \int_{-\infty}^{+\infty} pr(q, \phi) e^{(-i\xi q)} dq \\ &= \int_{-\infty}^{+\infty} \int_{-\infty}^{+\infty} W(q \cos(\phi) - p \sin(\phi), p \cos(\phi) + q \sin(\phi)) e^{(-i\xi q)} dp dq. \end{aligned} \quad (2.59)$$

Using the substitutions $q' = q \cos(\phi) - p \sin(\phi)$ and $p' = p \cos(\phi) + q \sin(\phi)$, so that $q = q' \cos(\phi) + p' \sin(\phi)$ and $p = p' \cos(\phi) - q' \sin(\phi)$, the expression simplifies to [1]

$$\tilde{pr}(\xi, \phi) = \int_{-\infty}^{+\infty} \int_{-\infty}^{+\infty} W(q', p') e^{(-i(q'\xi \cos(\phi) + p'\xi \sin(\phi)))} dp' dq', \quad (2.60)$$

remember the Jacobian for this substitution is one. This trick was useful as now the right side of the expression looks like Eq. (2.58) with $u = \xi \cos(\phi)$ and $v = \xi \sin(\phi)$. Then [1]

$$\tilde{pr}(\xi, \phi) = \tilde{W}(\xi \cos(\phi), \xi \sin(\phi)) \quad (2.61)$$

Now we can recover the Wigner function using the inverse Fourier transform over the characteristic function

$$W(q, p) = \frac{1}{4\pi^2} \int_{-\infty}^{+\infty} \int_0^\pi \tilde{W}(\xi \cos(\phi), \xi \sin(\phi)) |\xi| e^{i\xi(q \cos(\phi) + p \sin(\phi))} d\phi d\xi, \quad (2.62)$$

using polar coordinates [1]. Replacing the characteristic function with the definition in Eq. (2.61)

$$W(q, p) = \frac{1}{4\pi^2} \int_{-\infty}^{+\infty} \int_0^\pi \tilde{pr}(\xi, \phi) |\xi| e^{i\xi(q \cos(\phi) + p \sin(\phi))} d\phi d\xi \quad (2.63)$$

$$= \frac{1}{4\pi^2} \int_{-\infty}^{+\infty} \int_0^\pi \int_{-\infty}^{+\infty} pr(x, \phi) |\xi| e^{i\xi(q \cos(\phi) + p \sin(\phi) - x)} dx d\phi d\xi \quad (2.64)$$

$$= \frac{1}{2\pi^2} \int_0^\pi \int_{-\infty}^{+\infty} pr(x, \phi) K(q \cos(\phi) + p \sin(\phi) - x) dx d\phi, \quad (2.65)$$

where

$$K(x) = \frac{1}{2} \int_{-\infty}^{+\infty} |\xi| e^{i\xi x} d\xi \quad (2.66)$$

is known as the kernel [1]. From the Radon inverse transform, as the expression in Eq. (2.65) is known, it is evident that the Wigner function can be recovered from its marginal distributions or projections. However, it can also be reconstructed using only a sample of the projections [33].

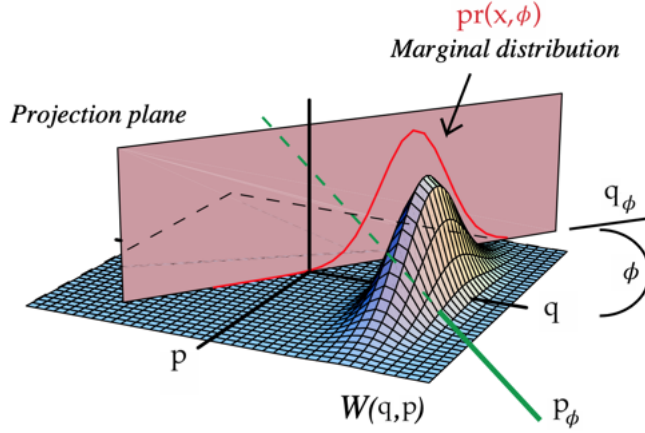


Figure 2.13: Wigner function $W(q, p)$ and its projections, the quadrature distributions $pr(x, \phi)$. The Radon inverse transform allows reconstruction of the Wigner function from its projections. Adapted from Ref. [19].

Filtered Back-projection Algorithm

From a numerical point of view, if Eq. (2.65) is going to be applied over measured quadrature distributions the Kernel expression Eq. (2.66) must be solved. This kernel amplifies high frequencies, because of the term $|\xi|$, making it unstable and has to be regularized in order to avoid ill behaviors [34]. The Filtered Back-projection Algorithm is an approach to solve this issue. It relays on a cutoff frequency k_c that keeps the kernel from diverging.

Introducing the k_c into the kernel expression in Eq. (2.66) [1]

$$\begin{aligned} K(x) &= \frac{1}{2} \int_{-k_c}^{+k_c} |\xi| e^{i\xi x} d\xi \\ &= \frac{1}{x^2} (\cos(k_c x) + k_c x \sin(k_c x) - 1), \end{aligned} \quad (2.67)$$

a more usable result is obtained. However, this expression diverges when $x = 0$. To solve this, the Taylor series expansion can be used [1]

$$K(x) = \frac{k_c^2}{2} \left(1 - \frac{k_c^2 x^2}{4} + \frac{k_c^4 x^4}{72} - \frac{k_c^6 x^6}{2880} + \dots \right). \quad (2.68)$$

To determine an appropriate value for k_c , it must be above the essential frequency band-width of W . It also is important to note that details in the reconstruction are inverse proportional to k_c , so higher values are not necessarily better [34]. With this regularization of the Kernel, the Wigner function can be computationally reconstructed by performing the integrals over the sampled data.

From Wigner function to density matrix

The Wigner function has a stretch relation to the density matrix, as expressed in Eq. (2.56). This relationship can be exploited to obtain an expression for the density matrix using only the Wigner function, through a Fourier transform over one of the components the relation obtained is [29]

$$\langle q + q' | \hat{\rho} | q - q' \rangle = \int_{-\infty}^{\infty} W(q, p) e^{2ipq'} dq'. \quad (2.69)$$

This relation yields the density matrix in the quadrature representation. To obtain the same in the photon number representation a change of basis is performed [15]

$$\langle n | \hat{\rho} | m \rangle = \frac{1}{\sqrt{\pi 2^n 2^m n! m!}} \int_{-\infty}^{\infty} \int_{-\infty}^{\infty} e^{-\frac{1}{2}(q^2 + q'^2)} H_n(q) H_m(q') \langle q | \hat{\rho} | q' \rangle dq dq', \quad (2.70)$$

where $H_k(x)$ are the Hermite polynomials of degree k .

C h a p t e r 3

COMPUTATIONAL SIMULATIONS

In this chapter, a computational-simulated perspective towards quantum tomography is presented. Quadrature distributions for the coherent, vacuum, squeezed and thermal states are simulated and quantum tomography is performed over them to reconstruct their respective Wigner functions. Afterward, the density matrix for each one of the states in the quadrature and Fock representation is recovered from the Wigner functions. The whole system put in place for the tomographic reconstruction and density matrix recovery is independent for the simulated data and can be used for real measurements. The implementation was developed in Python and a user-friendly graphical interface was put in place. More details can be found in appendices [A.1](#), [A.2](#), and [A.3](#).

3.1 Data generation

The quadrature distributions are simulated as the outputs of a balanced homodyne detector, in this sense the subtracted current described in Eq. [\(2.37\)](#) is the actually simulated quantity. To perform the simulation of the measurements, the properties for each state are used to predict the outcomes. The advantage of simulating the output of the balanced homodyne detector lays on the ability to test the tomography system for real measurements.

The quadrature distribution for a given phase ϕ should be centered in the expected value and according to Eq. [\(2.17\)](#) there should be a deviation from the center proportional to the uncertainty for the given quadrature. Using a normal distribution comes in naturally due to the *central limit theorem*. This theorem states that the sum of the mean values of samples over the same population would behave as a normal distribution [\[35\]](#). Remember the photodiodes used in balanced homodyne detection act as averaging devices and therefore the substracted current in Eq. [\(2.17\)](#) is an average. Therefore, multiple measurements of this current would be normally distributed.

The simulated data is constructed from sampling a random normal distribution centered in a given μ and with deviation a deviation σ , these samples simulate the current i_- for a given ϕ . Afterward, a histogram is constructed and fitted to a

Gaussian function. The resulting gaussian function would be the quadrature probability distribution. This technique, in contrast to obtaining the normal distributions directly by inputting μ and σ into the analytical description, allows some randomness and emulates better real-world simulated measurements. More samples taken account for a more precise approximation to the desire μ and σ , while fewer samples allow more variation. This process has to be repeated for different values of ϕ as it works only for a single phase. Figure 3.1 depicts a quadrature distribution obtained using this method. Ten-thousand samples were taken from a random distribution with $\mu = 5$ and $\sigma = 1$ fitted to a Gaussian function that ended up with $\mu = 4.976$ and $\sigma = 0.977$. Insights on the implementation of this process can be encounter in appendix A.1.

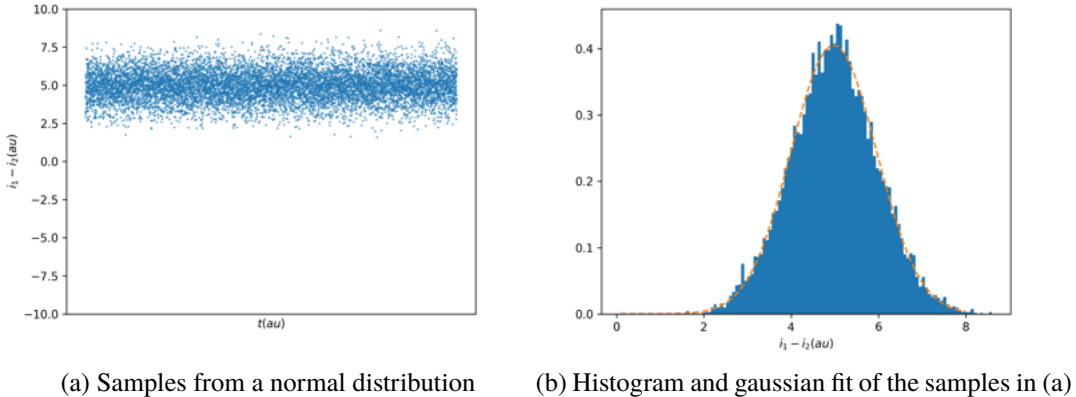


Figure 3.1: Process for obtaining simulated quadrature distributions. A normal distribution is sampled and then fitted. (a) are ten thousand random samples following a normal distribution with $\mu = 5$ and $\sigma = 1$. They can be interpreted as measurements of $i_1 - i_2$ over time. (b) resembles data from (a) in a histogram of 100 bins and the corespondent gaussian fit over the data. This fit would be used as the quadrature distribution for a given phase ϕ . The fit yields a gaussian with $\mu = 4.976$ and $\sigma = 0.977$.

Vacuum

To simulate the quantum quadrature distribution for the vacuum, the previous procedure is repeated a hundred times, one for a different phase. These phases are defined as equidistant values ranging from 0 to 2π . The quadratures are expected to always be centered at zero as there is no amplitude in this state, therefore $\mu = 0$ for all phases. σ can be found by its relation to the state uncertainty. According to Eq. (2.17) when the uncertainty is the minimum and equally distributed $\Delta p = \Delta q$,

then $\sigma^2 = (\Delta p)^2 = (\Delta q)^2 = \frac{1}{2}$. Having established that $\mu = 0$ and $\sigma = \frac{1}{\sqrt{2}}$ the simulation process is performed using these parameters.

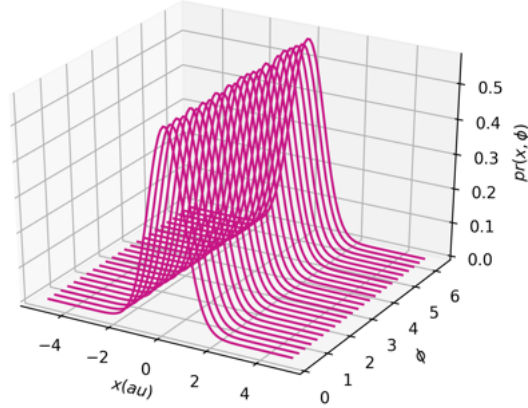


Figure 3.2: Simulated quadrature distributions for the vacuum state, using $\mu = 0$ and $\sigma = \frac{1}{\sqrt{2}}$ for every phase. By looking at the peaks it is evident that they are not equal, this accounts for the randomness introduced during the simulation process. Only 25 of the 100 simulated phases are portrayed.

Thermal

The thermal state is similar to the vacuum in the sense that both have average amplitude zero $\mu = 0$ for all phases, but they differ in the uncertainty as the thermal state is a not minimum uncertainty state. The deviation on the sampled normal distribution accounts for this, then σ can be chosen to a bigger value, in this case, $\sigma = 3$. An array of one hundred equidistant phases ranging from 0 to 2π is defined, and for each one of them the distribution is sampled and adjusted obtaining the result shown in Fig. 3.3.

Coherent

The data for the coherent state is generated using the same procedure used for the vacuum state, but this time the μ values have to change as they have to account for the amplitude α . An approach to understanding how the expected measurement from the homodyne detector is for a coherent state comes from Eq. (2.37) where it is clear that it behaves in a sinusoidal way. A sine function would yield all the amplitude in one of the quadratures, while a cosine would do the same in the other. A combination of both allows to distribute the amplitude into both quadratures. The values of μ

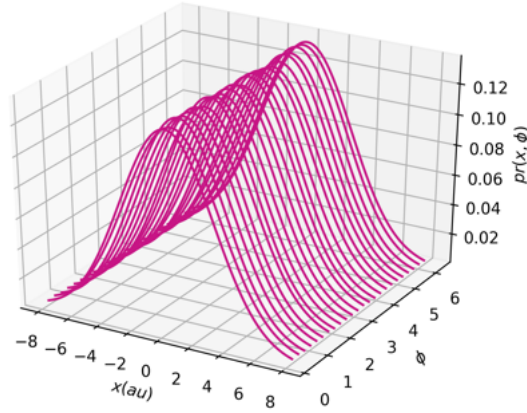
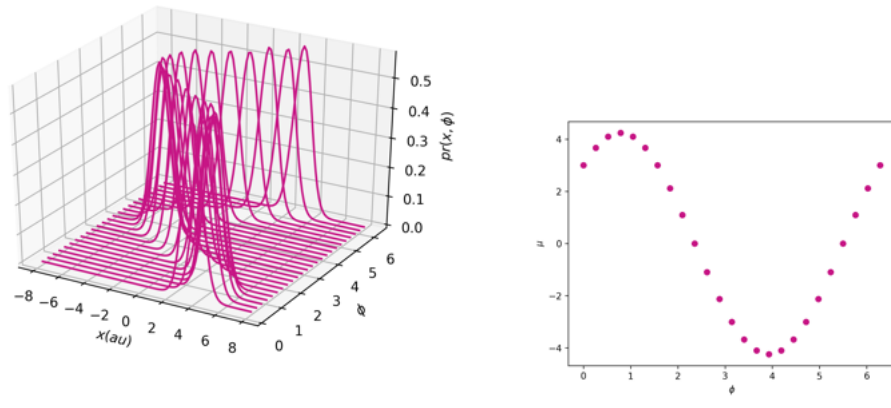


Figure 3.3: Simulated quadrature distributions for the thermal state using $\sigma = 3$. Only 25 of the 100 simulated phases are portrayed.

where distributed over the function $\mu(\phi) = (\cos(\phi) + \sin(\phi)) * Re(\alpha)$, meaning that both quadratures will have the same value $Re(\alpha) = Im(\alpha)$. One hundred values of ϕ evenly distributed between 0 and 2π were used, and for each phase $Re(\alpha) = 3$ and $\sigma = 0.7071$ were the parameters used to generate the distributions.



(a) Simulated quadrature distributions

(b) Averages from above

Figure 3.4: Simulated quadrature distributions for a coherent state with real and imaginary equal amplitudes $Re(\alpha) = Im(\alpha) = 3$. From above (b) it can be seen that the distributions follow a sinusoidal pattern.

Squeezed

Squeezed states can be squeezed on either quadrature, and they can either have an amplitude α , as the coherent states, or be the squeezed vacuum, with $\alpha = 0$. Three of these states were generated: the squeezed vacuum, the coherent squeezed in the p quadrature and the coherent squeezed in the q quadrature. To generate these states a function $\sigma(\phi)$ was created so that the deviation was dependent on the phase. This function follows the uncertainty principle, this can be achieved using the fact that these distributions are normalized. Any change in the width of the distribution would be compensated in the height. The σ values were distributed over a sinusoidal wave following the description of real squeezed measurements in Ref. [29]. Then, the states were generated as coherent and vacuum would normally be generated but using

$$\sigma(\phi) = \left(\sin(2(\phi + \eta) + 1) \frac{0.7}{2} \right) + \frac{1}{\sqrt{2}} - \frac{1}{4}, \quad (3.1)$$

this sine moves around $\sigma = \frac{1}{\sqrt{2}} + 0.1$ with a peak to peak amplitude amplitude of 0.7. To differentiate between the squeezing in the p quadrature and q quadrature, a shift η can be manipulated. $\eta = \pi/4$ corresponds to squeezing in p , $\eta = 3\pi/4$ corresponds to squeezing in q .

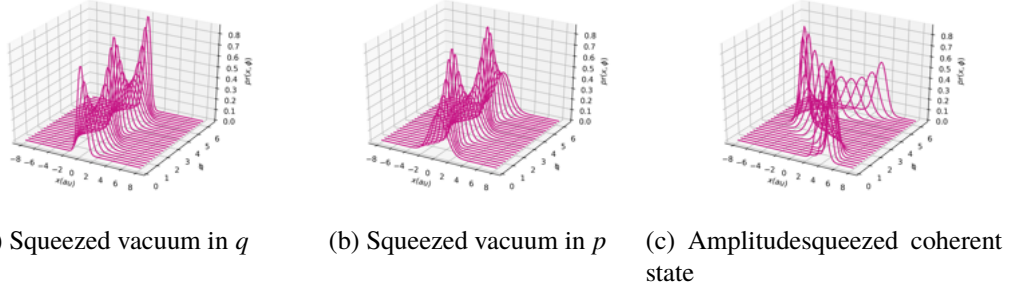


Figure 3.5: Simulated quadrature distributions for the squeezed vacuum using $\eta = 3\pi/4$ (a), squeezed vacuum using $\eta = \pi/4$ (b) and the squeezed amplitude coherent state using $\eta = \pi/2$ and $Re(\alpha) = Im(\alpha) = 3$.

3.2 Wigner reconstruction via quantum tomography

The Wigner function can be recovered from the marginal distributions of the quadratures according to Eq. 2.65 using the kernel approximation of the filtered back-projection algorithm in Eq. 2.67. A parameter γ is introduced to account for when to switch between Eq. 2.67 and the Taylor approximation in Eq. 2.68 [1]. When $\gamma \geq |k_c x|$ the Taylor approximation is used, otherwise Eq. 2.67 is used. γ

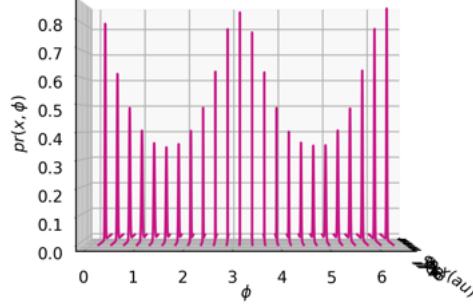


Figure 3.6: Side view of the simulated squeezed vacuum in Fig. 3.5, the sinusoidal height of the peaks is evident from this perspective.

was set to 0.01 for all the tomographic reconstructions performed in this chapter. The Radon inverse transform requires all of the projections for the reconstruction, but having the projections for one hundred phases and one hundred values in the projection for each phase, both equally distribute, has been proved to be enough samples to perform a tomography without significant error [29][34]. The integrals in Eq. 2.65 can be numerically performed by an approximation to the Riemann method. Multiprocessing is exploited for better performance, as there is no dependence between the values for different $W(q, p)$. Nearly five thousand values of q and p were used to reconstruct each Wigner function. More information on the implementation details can be found in A.2.

Vacuum

The vacuum state Wigner function was reconstructed using $k_c = 5$. The result is portrayed in Fig 3.7. It is shaped like a two-dimension gaussian and is centered in the origin, as expected. The result is comparable to the Wigner function presented in Fig. 2.12 and to the reconstructed Wigner function for real measured quadrature distributions of the vacuum state, such as the one obtained by Breitenbach in Ref. [36]. This Wigner function position and shape come in naturally, the center accounts for the amplitude most probable value, in this case, zero and the width indicates the uncertainty, which is minimum and symmetrical for this state.

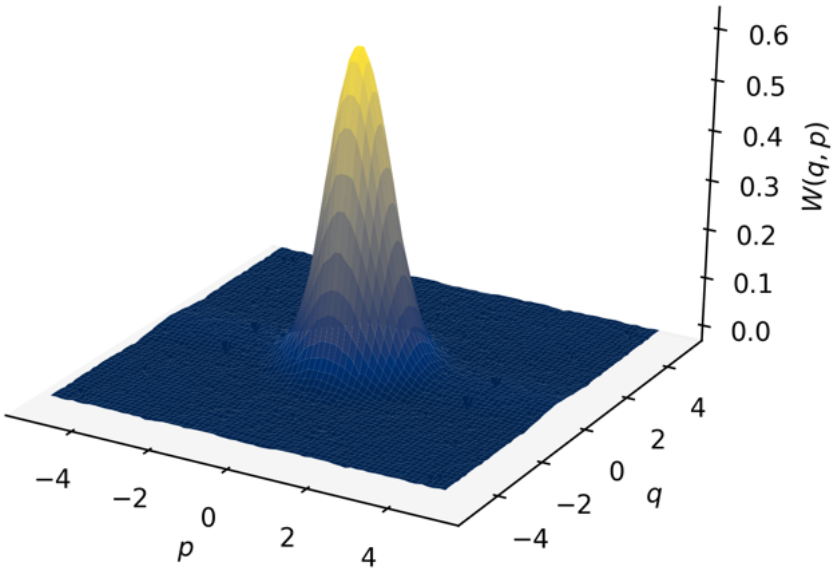


Figure 3.7: Wigner function for the vacuum state reconstructed via quantum tomography over simulated quadrature marginal distributions. A cutoff frequency $k_c = 5$ was used.

Coherent states

Three coherent states were simulated and the Wigner function for each of them was obtained using quantum tomography. The first of these states was simulated at 45° , having both the imaginary and real part of the amplitude equal to three (Fig. 3.8), this is the exact same data generated in section 3.1 for the coherent state. The Wigner function for this state looks alike to the vacuum $W(q, p)$ but displaced from the origin. This displacement is equally distributed in both axes as expected for a state with the same amplitude in both the imaginary and real parts. The Wigner function obtained resembles accurately the $W(q, p)$ from Fig. 2.12. In Fig. 3.9 two coherent states with only imaginary or real amplitudes are depicted. In this case, the Wigner function reflects this behavior by being displaced only in one of the axis.

Thermal state

A thermal state quadrature distributions were simulated as described in section 3.1 and the tomography process was performed over it. The result is depicted in Fig. 3.10. The $W(q, p)$ obtained for this state is centered at the origin and has a bigger width in comparison to the vacuum state. The bigger width indicates more uncertainty and the center indicates this state has zero amplitude on average. This behavior is as expected and matches the Wigner function for the thermal state in

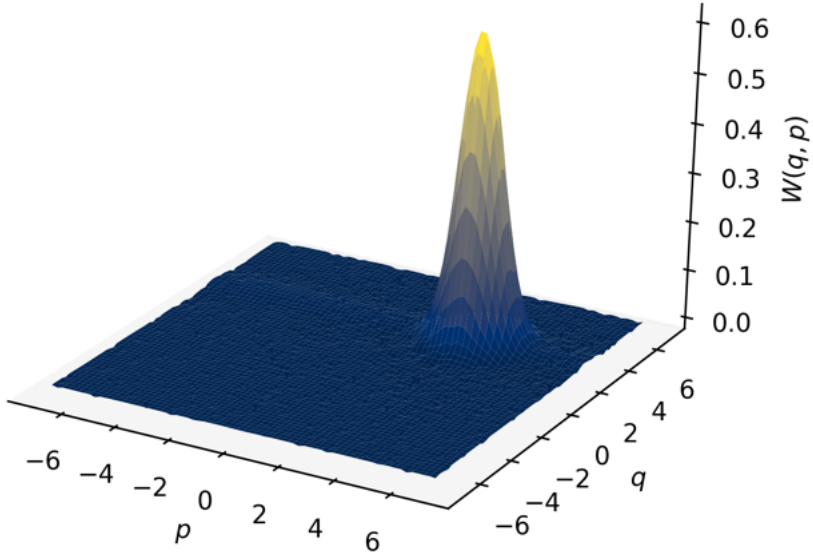


Figure 3.8: Wigner function for coherent state reconstructed via quantum tomography over simulated quadrature marginal distributions. In this case, both quadratures have the same value. A cutoff frequency $k_c = 5$ was used.

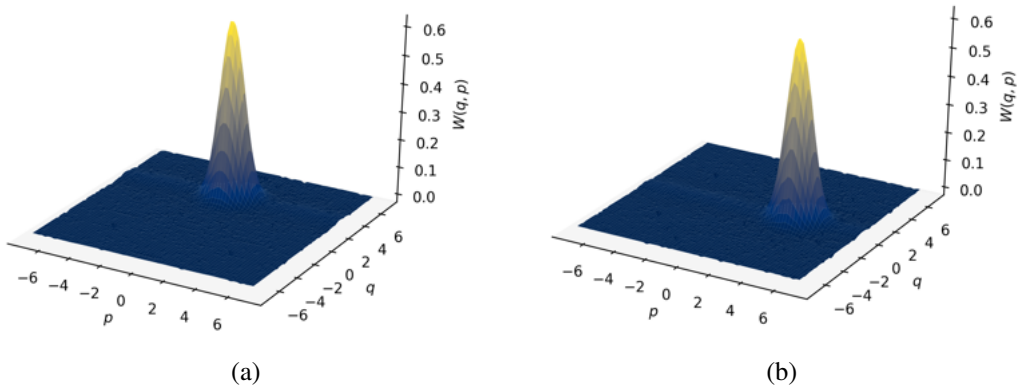


Figure 3.9: Wigner function for simulated coherent states with only real (b) or imaginary (a) amplitudes. Both were reconstructed using $k_c = 5$.

Fig 2.12.

Squeezed states

The Wigner functions for five different simulated squeezed states are presented. Four of them correspond to the squeezed vacuum and one to the amplitude squeezed coherent state. The first four differ from each other by the squeezing direction, this by means of changing the value of η from Eq. 3.1. The reconstructed Wigner

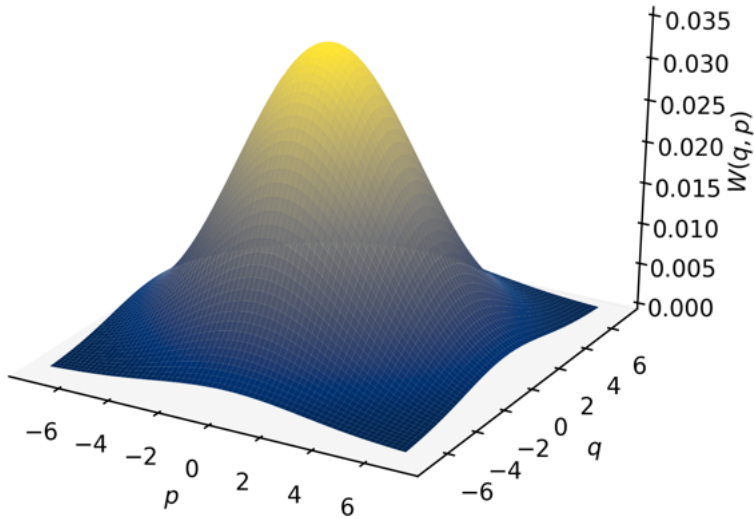


Figure 3.10: Wigner function for thermal state reconstructed via quantum tomography over simulated quadrature marginal distributions. The function is centered at the origin. A cutoff frequency $k_c = 1$ was used to perform the tomographic process.

functions for these states are centered at the origin, but they are not symmetrical as their uncertainty is not evenly distributed between both quadratures (Fig. 3.11). The $W(q, p)$ for a simulated amplitude squeezed coherent state can be found in Fig. 3.12. The Wigner function obtained for this state was the same as for the squeezed vacuum but moved from the origin.

All the Wigner functions reconstructed via quantum tomography from the simulated quadrature distributions fulfilled the expectations as they adjusted to the theory and moreover had shapes, positions, and widths that accounted for their properties. The algorithm used proved to be stable and suitable for performing this task by filtering the right amount of high frequencies by adjusting k_c . Tuning this parameter correctly is important as the quality of the results depend on it. The tuning has to be performed for each reconstruction and is going to depend on the essential frequency bandwidth of the resulting $W(q, p)$ [34]. In Fig. 3.13 the results of using big or small cutoff frequencies k_c is illustrated, in both cases the result is not smooth.

3.3 Density matrix recuperation

The density matrix in the quadrature representation can be recovered from the Wigner function using Eq. 2.69 and furthermore the density matrix in the Fock representation can be obtained using Eq. 2.70. Using the Wigner functions, from the previous section, obtained by performing tomography over the simulated dis-

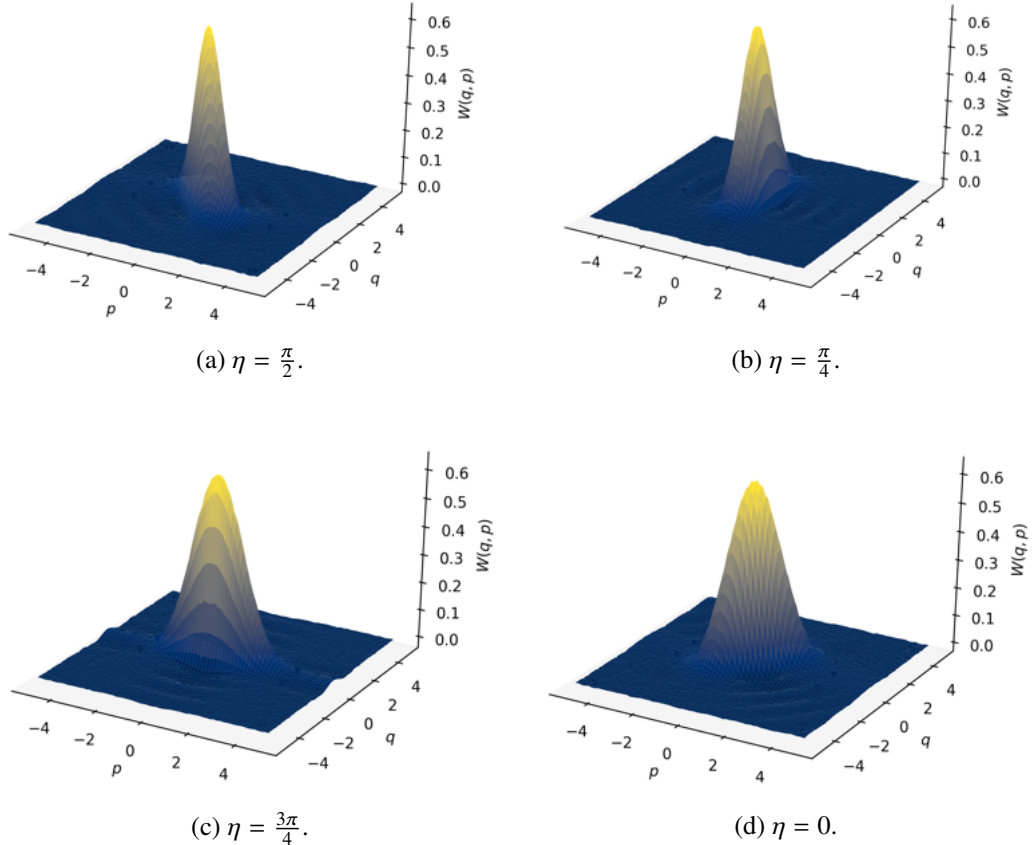


Figure 3.11: Wigner functions for the squeezed vacuum reconstructed via quantum tomography over simulated quadrature marginal distributions. All the functions are centered at the origin, but the squeezing is in a different direction. A cutoff frequency $k_c = 5$ was used to perform the tomographic process in all of them.

tributions generated in section 3.1, the density matrix in both representation was recovered for a diversity of states. Computational implementation details can be found in Appendix A.3.

Density matrix in the quadrature representation

Two density matrices were obtained for each state. One in the q, q' representation and another one in the p, p' representation. These matrices contain information about the value and uncertainty of p or p' , and therefore their relevance. To calculate them two versions of equation Eq. 2.69, one that integrates over q as the equation is; and another switching q for p . Distinguishing states is easier using the density matrix in the quadrature representation as their properties in each quadrature are isolated. The matrices presented in this section are portrayed using contour lines

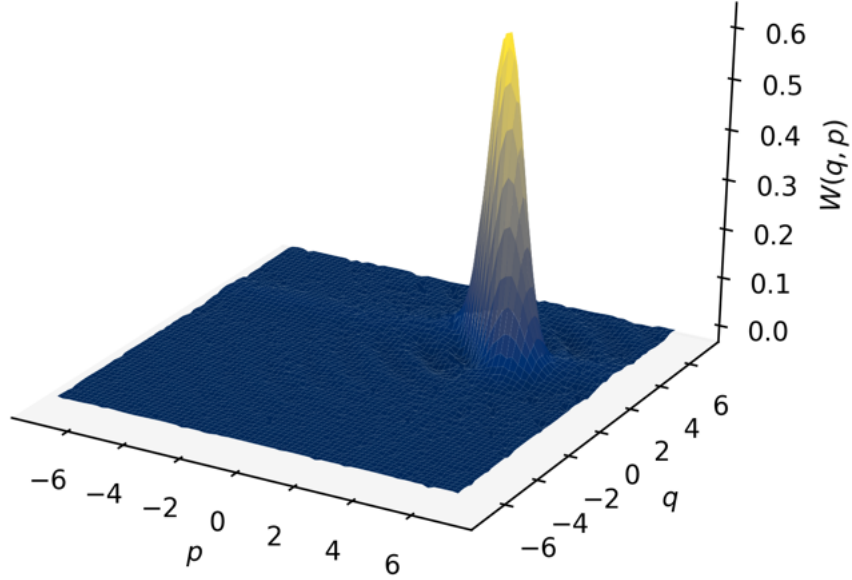


Figure 3.12: Wigner functions for the amplitude squeezed state reconstructed via quantum tomography over simulated quadrature marginal distributions using $\eta = \frac{\pi}{2}$. A cutoff frequency $k_c = 5$ was used.

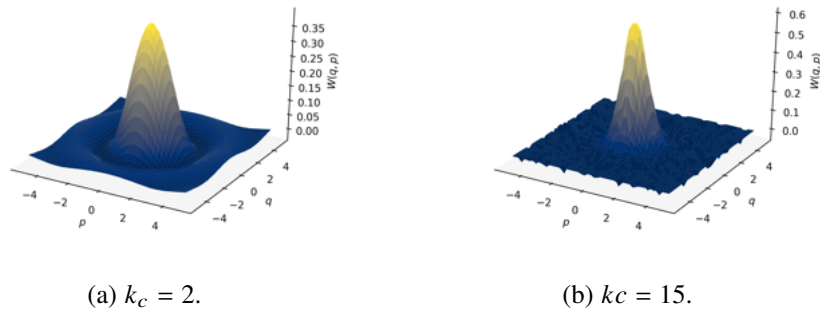


Figure 3.13: Tomographic reconstruction for the vacuum state using two different values of k_c . In both cases, the result is not smooth.

for their simplicity and because they serve the purpose of indicating where is the maximum of the function. The computational implementation uses interpolation to smooth the result and simplify the integration process, as the resulted data is not organized, for obtaining the density matrix in the Fock representation (see next section).

Vacuum

Using the Wigner function of the vacuum state in Fig. 3.7, the density matrix for the vacuum state was calculated for each quadrature. Figure 3.14 shows the results obtained. Both representations are equal, gaussian shaped functions centered at zero. The circular contour lines with increasing radius reflect their behavior. As diameters for contour lines at the same level are in the same position, the width and therefore the uncertainty is equal for both quadratures. This makes sense for this state as it is symmetrical and centered in the origin.

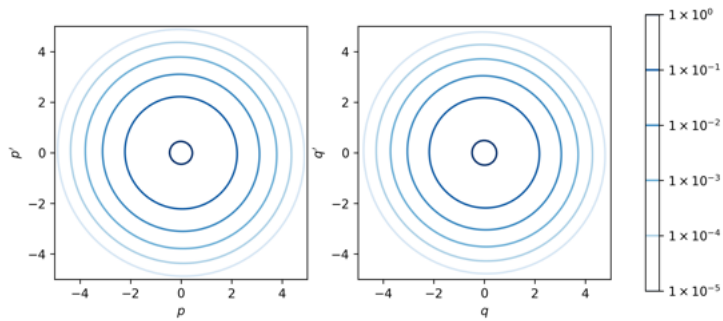
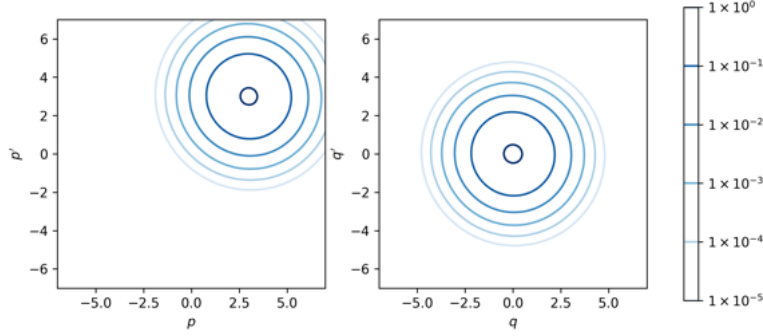


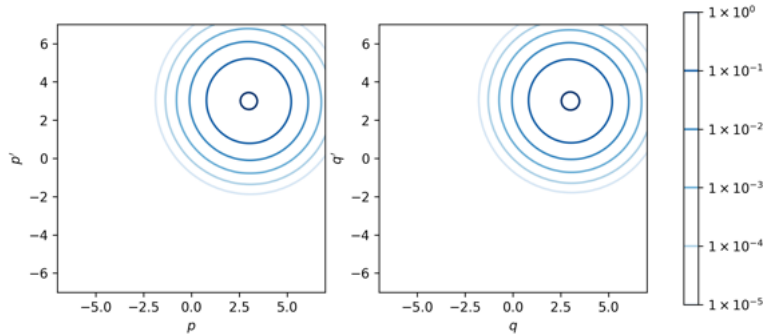
Figure 3.14: Density matrices in the quadrature representation for the simulated vacuum state. p representation is portrayed on the left side and q on the right side.

Coherent states

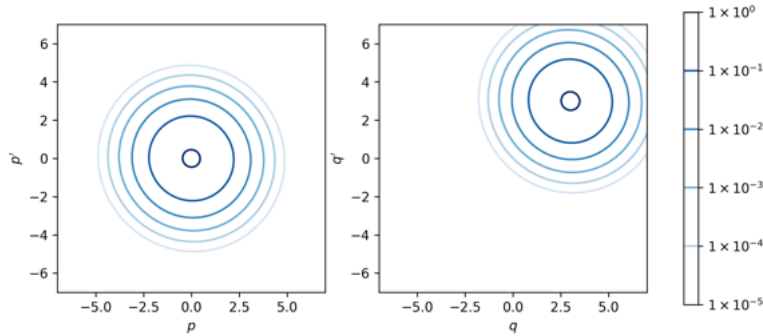
The density matrices for three different coherent states were calculated. The first one had all the amplitude in p , the second had all the amplitude in q and the last one had equal imaginary and real amplitudes, results are depicted in Fig 3.15. The matrices obtained for the first two were different for each quadrature as they had to account for differences in quadrature amplitudes. For the state with all the amplitude in p , $\langle q | \hat{\rho} | q' \rangle$ is centered at zero, while $\langle p | \hat{\rho} | p' \rangle$ is centered at three (which was the simulated amplitude). For the state with all the amplitude in q the opposite occurs. The state with equal amplitudes for both quadratures reflects this by centering both density matrices at the same point. For the three states, the uncertainty in both quadratures is equal, then the density matrices for both quadratures have the same width.



(a) Coherent state only with imaginary amplitude $Im(\alpha) = 3$. Wigner function for the same state can be found in Fig [3.9](a).



(b) Coherent state only with $Re(\alpha) = Im(\alpha) = 3$. Wigner function for the same state can be found in Fig [3.8].



(c) Coherent state only with real amplitude $Re(\alpha) = 3$. Wigner function for the same state can be found in Fig [3.9](b).

Figure 3.15: Density matrices in the p representation (left) and q (right) representation for three different coherent states.

Thermal states

The Wigner function for the thermal state from the previous section (Fig. [3.10]) looked similar to the vacuum state. It only differs in the width. Naturally, this

is the only difference between these two states' density matrices in the quadrature representation, see figure [3.16]. The thermal density matrices reflect the symmetry of the state, by having centers in the origin; but as the uncertainty is bigger than the one from the vacuum the diameter for the circular contour lines is bigger than the one for these lines at the same levels in the vacuum matrices. This makes sense as they are not minimum uncertainty states.

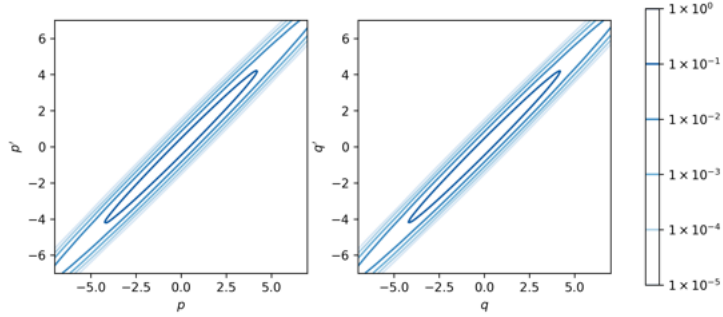


Figure 3.16: Density matrices in the quadrature representation, p in the left and q in the right, for the simulated thermal state.

Squeezed states

Squeezed states have different uncertainty for each quadrature and have turned relevant in recent years for their unique applications. Differentiating them and analyzing the amount of squeezing can be performed by comparing the density matrices in each quadrature representation. Two states are considered relevant to present in this section, the squeezed vacuums in each one of the quadratures. The matrices obtained are depicted in Fig. [3.17]. When the squeezing is in certain quadrature the contour lines come closer, while in the other quadrature they separate. This is the evidence of a squeezing state as it portrays different uncertainty for each quadrature. When the level of squeezing is larger the uncertainty is further reduced in one direction and expanded in the other. This is translated into more difference in the contour lines distances from the center. Note that the contour lines on the squeezed quadratures in Fig. [3.17] are closer to each other than the ones for the vacuum state in Fig. [3.14], this phenomenon indicates that uncertainty in a given quadrature is smaller than it would be for a vacuum state.

With the results from all the states above, the usefulness of the density matrix in the quadrature representation is clear as it allows to visualize each quadrature amplitude

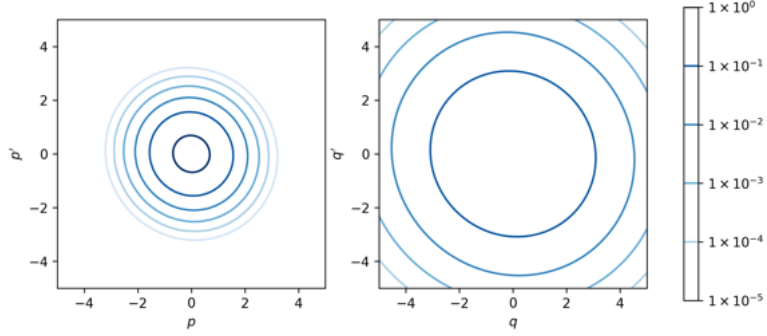
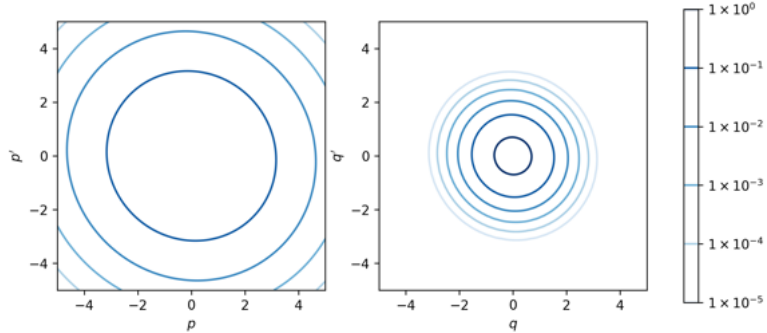
(a) Squeezed vacuum in the p quadrature.(b) Squeezed vacuum in the q quadrature.

Figure 3.17: Density matrices in the p representation (left) and q (right) representation for the squeezed vacuum.

and uncertainty in an easy -comprehensive- way. As a matter of fact, distinguishing squeezed states is easier using this representation [29]. The process for obtaining the density matrix in the quadrature representation is considered successful as the results adjust to the properties expected by following the theory for each state.

Density matrix in the Fock representation

The density matrix in the Fock representation is a common tool in photonics to represent states as its diagonal is directly related to the photon number probability. This representation can be obtained from the density matrix in the quadrature representation using Eq. 2.70. The values for the density matrix in the quadrature representation are easily integrated as they have previously been interpolated. These matrices were calculated for the vacuum, coherent, thermal, and squeezed states.

Vacuum

The density matrix in the number representation obtained for the simulated vacuum state is completely located in zero. This result makes sense as the expected number of photons for this state is zero. It is depicted in figure [3.18] and resembles accurately the analytical matrix in Fig. [2.9].

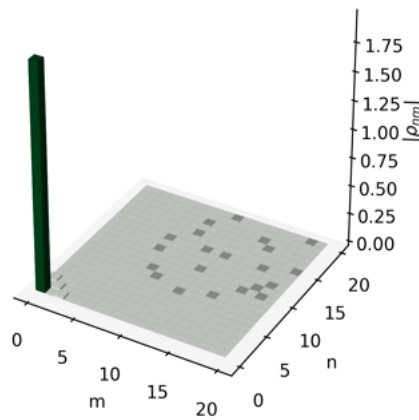


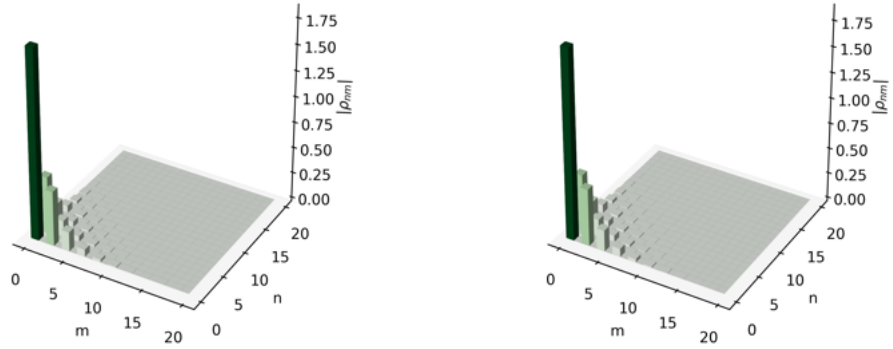
Figure 3.18: Density matrix in the Fock representation for the simulated vacuum state.

Squeezed states

When the simulated vacuum state is squeezed in one of its quadratures the obtained $\langle n | \hat{\rho} | n \rangle$ has non-zero values for even values of n and m around zero (Fig [3.19]). Equation [2.55] describes this behavior for the squeezed vacuum.

Thermal state

Furthermore, if the simulated vacuum state uncertainty is amplified symmetrically, yielding a thermal state, the density matrix in the Fock representation turns into a diagonal matrix. The calculated matrix is presented in figure [3.18]. The thermal state is a statistical mixture and its photon number probability tops at zero and decreases from there on, this behavior adjusts to the result obtained. That same behavior is the one analytically obtained in figure [2.7].



(a) Squeezed vacuum in the q quadrature. (b) Squeezed vacuum in the p quadrature.

Figure 3.19: Density matrices in the Fock representation for two different simulated squeezed vacuum states.

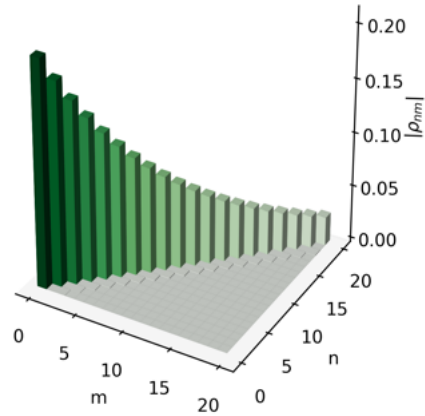


Figure 3.20: Density matrix in the number basis for the simulated thermal state.

Coherent state

Finally, when the simulated vacuum state is displaced from the origin, having a non zero average photon number, the coherent state is obtained. The density matrix in the number representation obtained for the coherent state was centered at a non zero value that decreases exponentially. The result is presented in Fig. 3.21.

In the four cases, the matrices obtained adjust to the shape of their correspondent

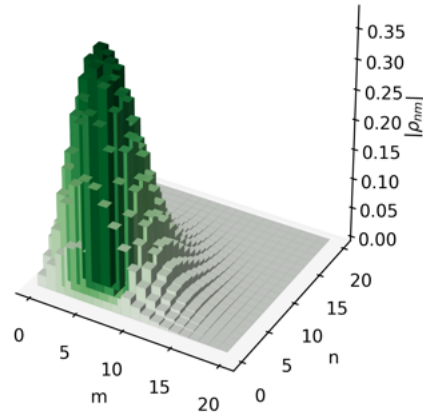


Figure 3.21: Density matrix in the Fock representation for a simulated coherent state with $Re(\alpha) = Im(\alpha) = 3$.

matrices from section 2.3. Accomplishing the recovering of the same properties expected for each of this state in the number representation, the process to perform the change of basis over the density matrix on the quadrature representation is accurate.

Chapter 4

EXPERIMENT

An initial experimental approach to balanced homodyne detection (BHD) is presented in this chapter. First, the optical set-up is explained. Then, it is followed by the electronic implementation of the subtractor used for BHD. Finally, the quadrature distributions for a coherent state are measured and the Wigner function is reconstructed via quantum tomography.

4.1 Optical set-up

The general schematic for the optical set-up for balanced homodyne detection is portrayed in Fig. 2.3, where the LO and the S are the input signals. S is the signal to be studied and LO the local oscillator. P_1 and P_2 are the photodiodes that produce currents i_1 and i_2 which temporal average, according to Eq. (2.37), allows to obtain information about the quadratures of S. PS is the phase sifter that permits the variation of the relative phase ϕ between LO and S, required to obtain the marginal distributions $pr(q, \phi)$ for different phases.

There are some considerations to account for in a real implementation on the optical table. The first of these considerations come in relation to the actually used components. For this implementation two high speed silicon photo diodes (FDS100) with optimal wavelength detection ranging from 350 – 1100nm, were used. This in accordance with the light source employed: a 633nm He – Ne laser with power close to 0.5mW. Finally, two lenses with 3mm focal length were used to focus light on the detectors. In this case, the LO and the Signal would correspond to the same source.

The second consideration regards the phase shifter. Multiple implementations use a single mirror over a piezo-electric mechanism to change the LO phase [8][16][31][37]. Although this is a simple intuitive way of performing the task, it may lead to the unalignment of the detector. Therefore, the phase shifter for the LO was implemented by mounting a double mirror into a piezo-electric platform. This allowed the mirrors to move simultaneously, guaranteeing fixed positions for the input and outputs of the shifter, avoiding the alignment of the whole schematic to be compromised.

Finally, one must consider that beam splitters are not completely insensitive to

polarization and therefore results in Eq. 2.18 and Eq. 2.19 may not hold true [16]. To solve this problem two half wave plates are introduced before the main beam splitter to tune the polarization's of the LO and S to be equal.

Fig. 4.1 is the updated schematic taking into account the actually used components, the phase shifter implementation, and the polarization balancing. The actual optical schematic implemented on the optical table correspond to this figure and is presented in Fig. 4.2.

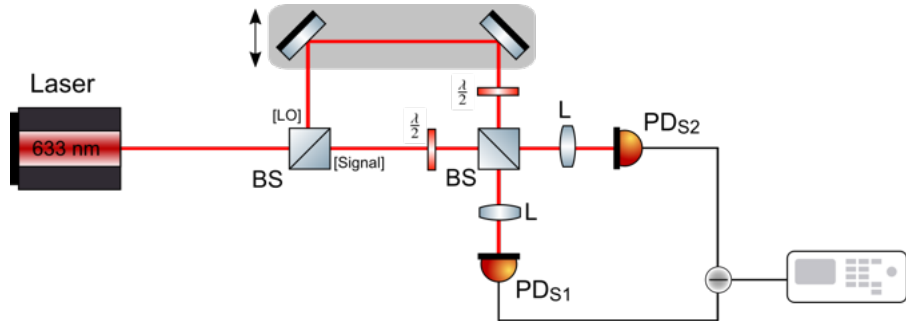


Figure 4.1: Schematic for the balanced homodyne detector. BS stands for beam splitter, L for lenses, PD for photodiode, and $\frac{\lambda}{2}$ for half wave plate. The doubled arrow specifies the movement of the piezo-electric.

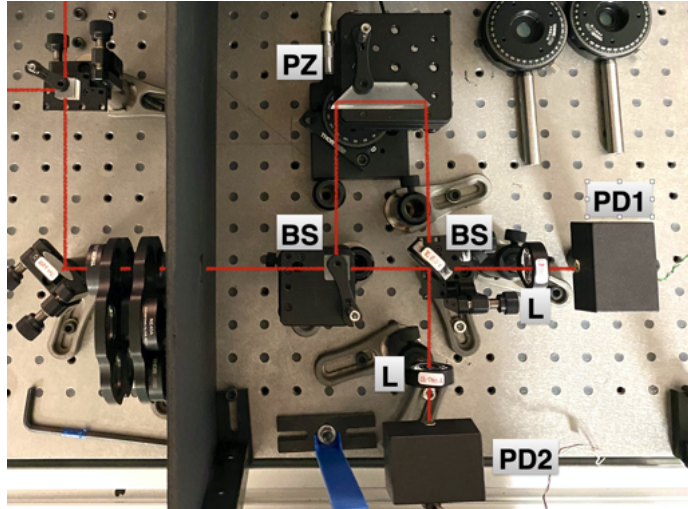


Figure 4.2: Implementation of the homodyne detector according to Fig. 4.1. Half wave plates are not in position.

4.2 Electronic set-up

Balanced homodyne detection requires subtraction of the detector outputs. This operation can be electronically implemented using operational amplifiers. The

subtraction device is incorporated before measuring in the scope. The diagram and implementation of the subtractor used are presented in figure 4.3. The first two local amplifiers act as amplifiers with gain equal to one, while the third amplifier subtracts according to the values of the resistors. If all resistors are set to the same value, there is no amplification.

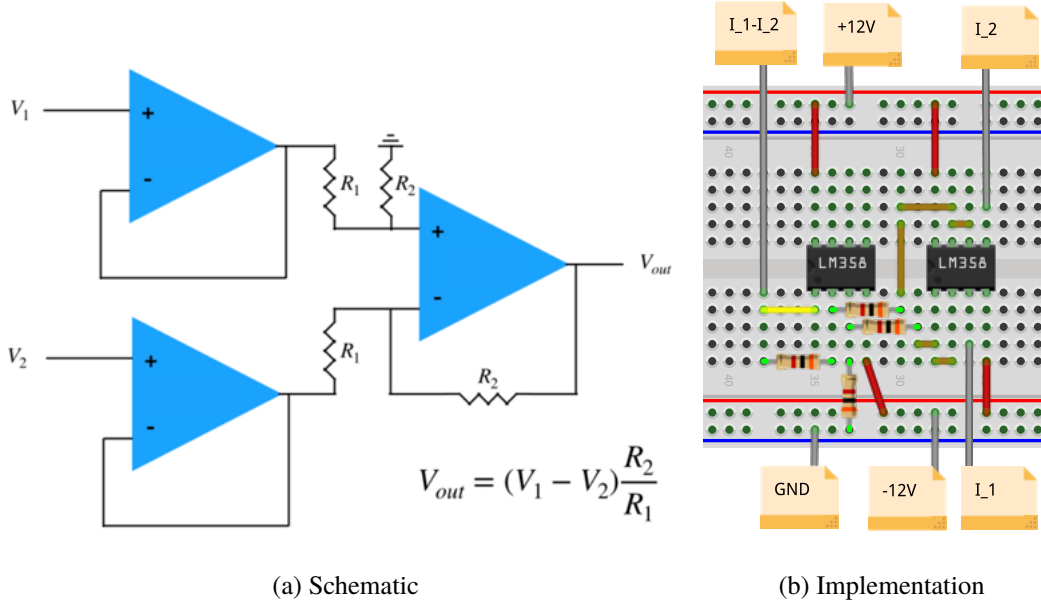


Figure 4.3: Subtractor using operational amplifiers. The schematic is on the left and the implementation using $3k\Omega$ resistors on the left.

This subtractor can be further improved to avoid amplifying (even with gain equal to one) before the real subtraction takes place. An example of such devices can be found in Ref. [2].

4.3 Measurements

Measurements for the coherent state were performed using the device described in the previous two sections. Before any measurement took place, the detectors were calibrated. This was done by exchanging their physical position and verifying that the measurement obtained is the same and does not depend on the detectors. A phase for the local oscillator was fixed by setting the piezo-electric to a given position. Then the scope recorded each photodiode output and the subtraction data for 2 seconds. An example of the data obtained during this process is shown in Fig. 4.4, the scope took ten thousand data points in 2 seconds. Then the data

was stored and the process repeated for a new position of the piezo-electric. The piezo-electric positions were increased by steps of $0.01\mu m$ until $0.6\mu m$.

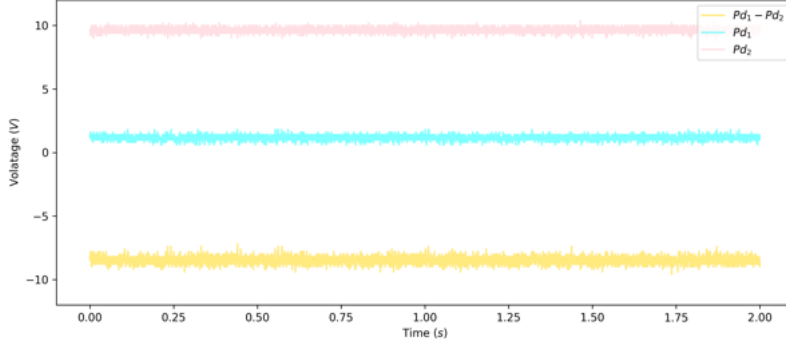


Figure 4.4: Measurements for the outputs of the photodiodes and their subtraction for a fixed LO phase.

Once the measurements were completed the data for each piezo position was organized in histograms and fitted to a gaussian function. This process would lead to the marginal distributions $pr(x, \theta)$ and it was the same as with the simulated data presented in the previous chapter. The averages obtained for this normal distributions were then plotted. The results are presented in figure 4.5, alongside a sinusoidal fit to show their behavior. This result is very similar to the simulated data for this state shown in Fig. 3.4, as the sinusoidal pattern related to coherent states, is present.

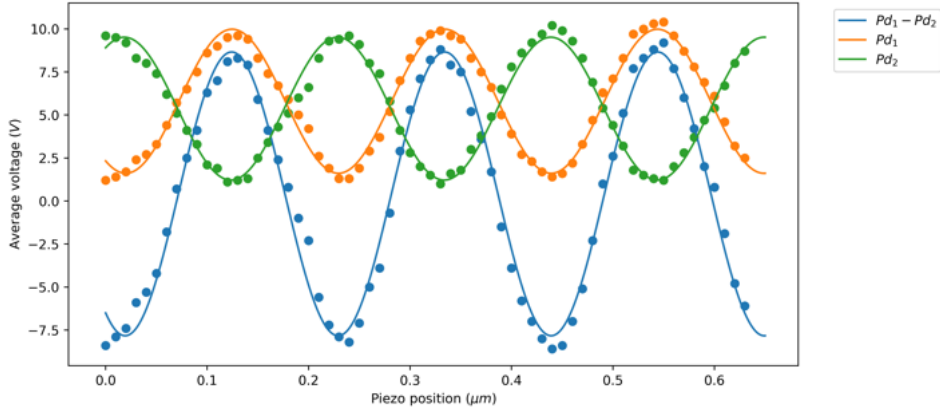


Figure 4.5: Averages of signals at both photodiodes and their subtraction for different piezo-electric positions. The three amounts follow a sinusoidal shape.

The piezo position can be converted to be the LO phase simply by choosing a full interference cycle, as this is equivalent to a change in phase from 0 to 2π . This is done

by mapping each $\Delta x = 0.01 \mu m$ to be $\Delta\phi = \frac{\pi}{12}$. Now the measurements correspond to a phase ϕ and, as they correspond to the $pr(x, \phi)$, we have the quadrature marginal distributions for a set of phases $pr(q, \theta)$. In Fig. 4.6 the measured quadratures partial probability distributions for each measured phase are presented. As expected and commented for Fig. 4.5 the behavior of the averages is sinusoidal. However, the heights of the distributions do not correspond to what is theoretically expected, the same height for all them. As distributions are normalized the height is related to the deviation, which at the same time relates to the uncertainty of the state. In Fig. 4.6 (b) it is evident that the heights do not follow a sinusoidal pattern either, so their behavior is not squeezed like as it was shown in figure 3.6 for a simulated squeezed state.

This erratic behavior on the uncertainty for this distribution most likely accounts for some kind of ill procedure during the measurement. Two possible causes are

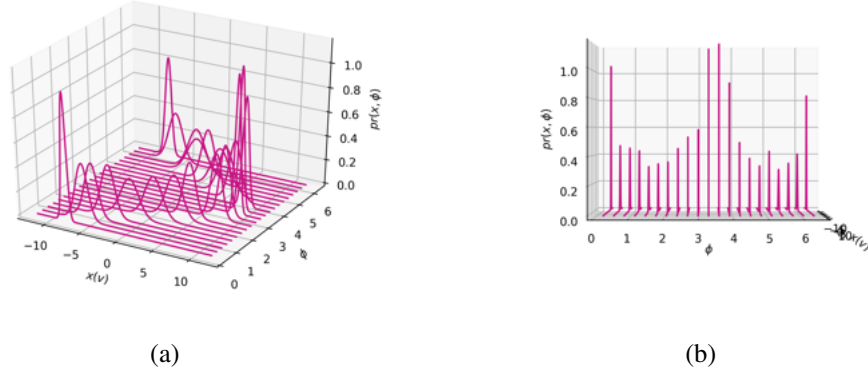


Figure 4.6: Quadrature marginal distributions measured for a coherent state. (a) and (b) are the same graphic from different angles.

explored. The first one is related to the intrinsic discrete operation of the oscilloscope used and the second one to the amplitude of the LO. Oscilloscopes capture data at discrete intervals, as they rely on finite memory. When measurements take place at faster rates the scope uses fewer intervals to perform better and makes data fall into fixed positions that alter their real distribution. This can be improved by decreasing the number of measurements per unit of time. The measurements presented above had only a precision of $0.1V$ as five thousand measurements were being recorded per second. The second possible cause is in regard to a strong local oscillator. For our measurements, the intensity of the LO is of the same order as the signal to be analyzed. However, for correct performance of the homodyne detector, it is

necessary to have an LO much stronger in intensity than S [1][2][3][17]. Therefore it is natural to think that our set-up can be improved by incorporating a neutral density filter in the S input. Furthermore, other causes such as frequency dependant noise can be explored by analyzing the measurements in frequency by the means of a spectrum analyzer [16].

4.4 Tomography

To performed quantum experimental tomography the measured quadrature marginal distributions reported in the previous section. The same process used in chapter three was used, but instead of using simulated data real measured data was used. The obtained Wigner function for these measurements is presented in figure 4.7. In figure 4.7(a) the gaussian behavior of a coherent state is clearly observed, this behavior is the same as the theoretical for this type of state as it can be seen in Fig. 2.12. Reported measurements of similar states display the same behavior [36]. In figure 4.7(b) a view from above of (a) is shown, depicting that the center of the distribution is displaced from the origin as expected for a coherent state. Nonetheless, its width is not evenly distributed and there is a lot of noise around the main function. The lines that go out of the high hill can be explained as the amount phases used is low (24) in comparison to the simulated coherent state (100). The noise closer to the main hill is more related to the non-symmetric distribution of the uncertainty over the whole 2π phase shift in the $pr(x, \phi)$. It is as if the algorithm is trying to reconstruct an object that does not look the same from different angles. Following

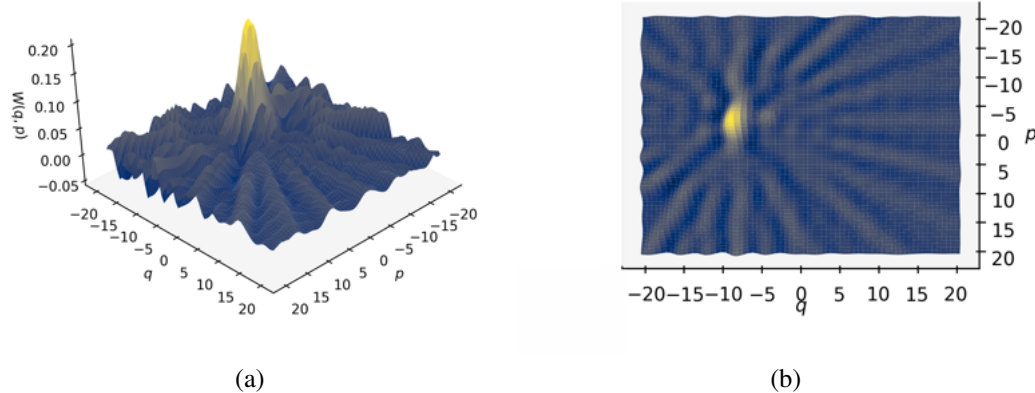


Figure 4.7: Wigner function reconstructed via quantum tomography for a coherent state measured using balanced homodyne detection. Cutoff frequency $k_c = 2$ was used.

the results and their sinusoidal shape for different phases, see Fig. 4.5, the obtained Wigner for these measurements adjust right to this coherent state but it has as it can be position in the specific value of q and p displaced from the origin. It is not a very well behaved gaussian function as the uncertainties from the measurements are not right.

Chapter 5

CONCLUSIONS AND PERSPECTIVES

In this work a system to perform quantum tomography in continuous variables, and furthermore obtain density matrices in the quadrature and Fock representation, was put in place and tested for simulated quadrature distributions for four different states of light: vacuum, coherent thermal and squeezed. The results presented in chapter three show that this algorithm is behaving well and is able to reconstruct the expected Wigner functions for all the states of light tested. The density matrices obtained in the quadrature and Fock representation for the vacuum, coherent, thermal, and squeezed states portrayed the physical behavior they are expected to display according to the theory. In this sense, a full computational process for recovering the Wigner function and density matrices in different representations was demonstrated. Furthermore, a careful analysis frequency dependant noise must be explored.

An initial approximation towards performing balanced homodyne detection was presented. The optical and electronic set-up were tested and measurements for the coherent state were performed. These measurements were correctly adjusted for the coherent state, but their uncertainty was ill-behaved. Possible causes and further improvements were detected to improve these measurements. Among them are increasing the power of the LO in contrast to the power of the S and increasing the precision of the scope measurements.

The experimental tomographic process was successful as a gaussian shape liked function displaced for the origin was obtained. This function portrayed most of the characteristics expected for a coherent state. However, its uncertainty was not evenly distributed. This accounts for the details of the measurements mentioned before.

The theory to understand quadrature representation, balanced homodyne detection and quantum tomography, and their implementation was detailed and introduced for tenderfoot readers. Furthermore, all the guidelines to perform the process are contained on the appendices of this work.

BIBLIOGRAPHY

- ¹U. Leonhardt, *Measuring the quantum state of light* (Cambridge University Press, 1997).
- ²A. M. Fox, *Quantum optics: an introduction*, First Edition (Oxford University Press, 2006).
- ³A. I. Lvovsky, and M. G. Raymer, “Continuous-variable optical quantum-state tomography”, *Reviews of Modern Physics* **81**, 299–332 (2009).
- ⁴O. Haderka, V. Michálek, V. Urbšek, and M. Ježek, “Fast time-domain balanced homodyne detection of light”, *Applied Optics* **48**, 2884 (2009).
- ⁵R. E. Slusher, L. W. Hollberg, B. Yurke, J. C. Mertz, and J. F. Valley, “Observation of squeezed states generated by four-wave mixing in an optical cavity”, *Phys. Rev. Lett.* **55**, 2409–2412 (1985).
- ⁶L.-A. Wu, H. J. Kimble, J. L. Hall, and H. Wu, “Generation of squeezed states by parametric down conversion”, *Phys. Rev. Lett.* **57**, 2520–2523 (1986).
- ⁷I. Khan, D. Elser, T. Dirmeier, C. Marquardt, and G. Leuchs, “Quantum communication with coherent states of light”, *Philosophical Transactions of the Royal Society A: Mathematical, Physical and Engineering Sciences* **375**, 20160235 (2017).
- ⁸D. T. Smithey, M. Beck, J. Cooper, and M. G. Raymer, “Measurement of number-phase uncertainty relations of optical fields”, *Physical Review A* **48**, 3159–3167 (1993).
- ⁹J. R. Álvarez, “Coherence-based quantum random number generator”, MA thesis (ICFO-Institut de Ciéncies Fotóniques, The Barcelona Institute of Science and Technology, 08860 Castelldefels (Barcelona), Spain, 2018).
- ¹⁰J. R. Álvarez, S. Sarmiento, J. A. Lázaro, J. M. Gené, and J. P. Torres, “Random number generation by coherent detection of quantum phase noise”, *Opt. Express* **28**, 5538–5547 (2020).
- ¹¹C. F. McCormick, A. M. Marino, V. Boyer, and P. D. Lett, “Strong low-frequency quantum correlations from a four-wave-mixing amplifier”, *Physical Review A* **78** (2008) [10.1103/physreva.78.043816](https://doi.org/10.1103/physreva.78.043816).
- ¹²J. Aasi, et al., “Enhanced sensitivity of the ligo gravitational wave detector by using squeezed states of light”, *Nature Photonics* **7**, 613–619 (2013).
- ¹³C. Cohen-Tannoudji, B. Diu, and F. Laloë, *Quantum mechanics* (Wiley, 2005).
- ¹⁴M. Hillery, R. O’Connell, M. Scully, and E. Wigner, “Distribution functions in physics: fundamentals”, *Physics Reports* **106**, 121–167 (1984).

- ¹⁵M. Beck, D. T. Smithey, and M. G. Raymer, “Experimental determination of quantum-phase distributions using optical homodyne tomography”, *Phys. Rev. A* **48**, R890–R893 (1993).
- ¹⁶A. Zavatta, M. Bellini, P. L. Ramazza, F. Marin, and F. T. Arecchi, “Time-domain analysis of quantum states of light: noise characterization and homodyne tomography”, *Journal of the Optical Society of America B* **19**, 1189 (2002).
- ¹⁷H.-A. Bachor, and T. C. Ralph, *Guide to experiments in quantum optics*, Second, Revised and Enlarged Edition (WILEY-VCH, 2009).
- ¹⁸M. Beck, *Quantum mechanics (theory and experiments)* (Oxford University Press, 2012).
- ¹⁹G. Breitenbach, “Quantum state reconstruction of classical and non classical light and cryogenic opto-mechanical sensor for high-precision interferometry”, PhD thesis (Universität Konstanz, June 1998).
- ²⁰H. P. Yuen, and V. W. S. Chan, “Noise in homodyne and heterodyne detection”, *Opt. Lett.* **8**, 177–179 (1983).
- ²¹G. L. Abbas, V. W. S. Chan, and T. K. Yee, “Local-oscillator excess-noise suppression for homodyne and heterodyne detection”, *Opt. Lett.* **8**, 419–421 (1983).
- ²²C. C. Gerry, and P. L. Knight, *Introductory quantum optics* (Cambridge Univ. Press, 2008).
- ²³L. Mandel, and E. Wolf, *Optical coherence and quantum optics*. (Cambridge University Press, 1995).
- ²⁴U. Leonhardt, *Essential quantum optics : from quantum measurements to black holes*. (Cambridge University Press, 2010).
- ²⁵A. Furusawa, *Quantum states of light* (Springer, 2015).
- ²⁶M. O. Scully, and M. S. Zubairy, *Quantum optics* (Cambridge University Press, 1997).
- ²⁷E. Wigner, “On the quantum correction for thermodynamic equilibrium”, *Physical Review* **40**, 749–759 (1932).
- ²⁸J. Bertrand, and P. Bertrand, “A tomographic approach to wigner’s function”, *Foundations of Physics* **17**, 397–405 (1987).
- ²⁹D. T. Smithey, M. Beck, M. G. Raymer, and A. Faridani, “Measurement of the wigner distribution and the density matrix of a light mode using optical homodyne tomography: application to squeezed states and the vacuum”, *Physical Review Letters* **70**, 1244–1247 (1993).
- ³⁰K. Vogel, and H. Risken, “Determination of quasiprobability distributions in terms of probability distributions for the rotated quadrature phase”, *Phys. Rev. A* **40**, 2847–2849 (1989).

³¹A. Zavatta, S. Viciani, and M. Bellini, “Quantum-to-classical transition with single-photon-added coherent states of light”, (2004).

³²J. Radon, “Über die bestimmung von funktionen durch ihre integralwerte längs gewisser mannigfaltigkeiten”, Berichte über die Verhandlungen der Königlich-Sächsischen Akademie der Wissenschaften zu Leipzig, Mathematisch-Physische Klasse (1917).

³³F. Natterer, *The mathematics of computerized tomography* (Wiley, 1986).

³⁴G. R. Roach, *Inverse problems and imaging* (Longman Scientific & Technical, 1991), pp. 68–102.

³⁵G. Pólya, “Über den zentralen grenzwertsatz der wahrscheinlichkeitsrechnung und das momentenproblem”, *Mathematische Zeitschrift* **8**, 171–181 (1920).

³⁶G. Breitenbach, S. Schiller, and J. Milynek, “Measurement of the quantum states of squeezed light”, (1997).

³⁷S. Grandi, A. Zavatta, M. Bellini, and M. G. A. Paris, “Experimental quantum tomography of a homodyne detector”, *New Journal of Physics* **19**, 053015 (2017).

Appendix A

COMPUTATIONAL IMPLEMENTATION

The computational implementation of the work described in Chapter 3: data simulation, tomographic reconstruction and density matrix calculation; was done in *Python 3*, using its numeric library *Numpy* and the graphics module *Matplotlib*. The parallelizing tool *Numba* for *Numpy* functions was used alongside direct parallelization techniques. The source code can be found at <https://github.com/amartinez1224/quantum-tomography>.

```

1 # Math tools
2 import numpy as np
3 from scipy import interpolate
4 from scipy.optimize import curve_fit
5 from scipy.special import gamma, factorial, hyp1f1, eval_hermite
6
7 # Plotting
8 import matplotlib.pyplot as plt
9 from mpl_toolkits.mplot3d import Axes3D
10 import matplotlib.colors as colors
11 import matplotlib.cm as cm
12
13 # Parallelization
14 from threading import Thread, Lock
15 from queue import Queue
16 import numba
17 from numba import jit

```

Listing A.1: Imports

A.1 Data generation

Data was generated using three arrays. One contained the ϕ values, other the μ values and the last one contained the σ values. All of them had the same size. The first one was generated with one hundred values evenly distributed between 0 and $\pi/2$. The second one depended on the type of light, either constant at zero or in a sinusoidal shape. The third one was either constant (non squeezed light) or sinusoidal (squeezed light).

```

1 phi = np.linspace(0,2*np.pi,100)

```

```

2
3 # Vacuum
4 mus = np.zeros_like(phi)
5 sig = np.zeros_like(phi)+(1/np.sqrt(2))
6
7 # Coherent
8 alpha=3
9 sig = np.zeros_like(phi)+(1/np.sqrt(2))
10 # At 45 deegres
11 mus = (np.sin(phi)+np.cos(phi))*alpha
12 # At 0 deegres
13 mus = np.sin(phi)*alpha
14 # At 90 deegres
15 mus = np.cos(phi)*alpha
16
17 #Thermal
18 mus = np.zeros_like(phi)
19 sig = np.zeros_like(phi)+3
20
21 #Squeezed
22 eta = 2*np.pi/4
23 sig = ((np.sin(2*(phi+(eta)))+1)*0.5*(1/np.sqrt(2)))+(1/np.sqrt(2))
   )-0.25
24 # Squeezed coh at 45 deegres
25 mus = (np.sin(phi)+np.cos(phi))*alpha
26 # Squeezed vac
27 mus = np.zeros_like(phi)
28
29 #Simulate state. m is a matrix where lines correspond to the
   marginal distributions for a given phi and x are the values
   where this distributions are sampled. np.size(m)=np.size(phi)*
   np.size(x)
30 m,x = gen(mus,sig,v1=-8,v2=8)

```

Listing A.2: Simulation of quadrature marginal distributions for different states.

```

1 def gen(mus,sig,density=100,v1=-12,v2=12):
2     # Matrix where distributions are stored
3     m=np.zeros((np.size(mus),density))
4     # Points to sample distribution
5     y=np.linspace(v1, v2, density)
6     for i in range(np.size(mus)): # Iterates over each phase
7         # Samples random normal distribution 10000 times
8         r = np.random.normal(mus[i],sig[i],10000)

```

```

9     # Creates hist
10    n,bins=np.histogram(r,bins=density,density=True)
11    # Fits hists and obtains arguments
12    arguments = gausshist(n, bins)
13    m[i,:]=gauss(y,arguments[0],arguments[1],arguments[2])
14    return m,y

```

Listing A.3: Generation of quadrature marginal distributions.

```

1 # 1d definition of a gaussian function
2 @jit(nopython=True, parallel=True)
3 def gauss(x, amp, mu, sig):
4     return amp*np.exp(-(x-mu)**2/(2.*sig**2))

```

Listing A.4: One dimensional gaussian function.

```

1 def gausshist(n, bins):
2     # Get bins centers
3     x = (np.abs(bins[1:]-bins[:-1])/2)+bins[:-1]
4     # Perform gaussian fit over histogram
5     arguments, variance = curve_fit(gauss, x, n, p0=[0.5,np.mean(x),
6     ),np.std(x)])
6     return arguments

```

Listing A.5: Fitting histogram to gaussian function.

Afterward the data can be plotted or stored.

```

1 fig = plt.figure()
2 ax = fig.add_subplot(111, projection='3d')
3 for i in range(np.size(phi)-1,0,-1):
4     ax.plot(x, np.zeros_like(x)+phi[i], m[i,:], c='mediumvioletred')
5 ax.set_ylabel(r"\phi$")
6 ax.set_xlabel(r"x(v)$")
7 ax.set_zlabel(r"pr(x,\phi$)")
8 plt.show()

```

Listing A.6: Plot generated data.

```

1 with open("m.dat", "wb") as f:
2     f.write(m.tobytes())
3 with open("phi.dat", "wb") as f:
4     f.write(phi.tobytes())
5 with open("x.dat", "wb") as f:

```

```
6     f.write(x.tobytes())
```

Listing A.7: Store data.

```
1 def loadData(mf="m.dat", phif="phi.dat", xf="x.dat"):
2     m = None
3     phi = None
4     x = None
5     with open(xf, "rb") as f:
6         x = np.frombuffer(f.read(), 'float64')
7     with open(phif, "rb") as f:
8         phi = np.frombuffer(f.read(), 'float64')
9     with open(mf, "rb") as f:
10         m = (np.frombuffer(f.read(), 'float64')).reshape((np.size(n),
11                                         np.size(x)))
12
13     return m, phi, x
```

Listing A.8: Read data.

A.2 Tomography

The radon inverse transform from Eq. 2.65 can be independently calculated for different pairs of values of q, p as there is no dependence between different pairs. Taking this into account, a parallelization scheme was set in place. This scheme consisted of having a queue where tasks are appended, then workers take the tasks from the queue and perform them. Workers are threads that run simultaneously on different cores, allowing parallelization. Tasks, in this case, are the $W(q, p)$ for fixed values of q and p . A Global variable W was created to store the full Wigner function and was accessed by all the workers at the same time as they had no collision issues because they calculate different positions $W(q, p)$ (for different values of q and p). There was no need to set *locks* over this variable.

```
1 # List of tasks to be done
2 que = Queue()
3
4 # Variable to store Wigner function
5 W = None
6
7 # Define workers
8 def worker():
9     # Repeat forever
10    while True:
11        item = que.get() # Get tasks
12        tomography(*item) # Perform task
```

```

13     # Inform the queue that a given task was completed
14     que.task_done()
15
16 # Number workers, it can be set to two times the number of cores
17 # available in the computer (each processor usually has two
18 # cores)
19 n=8
20 # Create workers
21 for i in range(n):
22     t = Thread(target=worker) # Create worker thread
23     t.daemon = True
24     t.start() # Launch worker

```

Listing A.9: Parallelization scheme.

Then tomography was performed in two steps. The first one consisted on filling the queue with all the correspondent tasks: values were the Wigner function was going to be calculated. The second one is that each worker performed Eq. 2.65 for its assigned tasks. Function *tomo* was in charge of filling the queue, it required the minimum and maximum values for q and p (*qMin*,*qMax*,*pMin*,*pMax*), how many values to generate between them (*density*), a cutoff frequency k_c and the data from the partial distributions (*m*,*phi*,*x*). The function *tomography* was in charge of obtaining the $W(q, p)$ values it required the q and p values, the data from the partial distributions (*m*,*phi*,*x*) and a cutoff frequency k_c . This function had to have two extra parameters *iq* and *ip* that were the positions (indices) from the matrix *W* where the $W(q, p)$ was going to be located. The data of the marginal distributions *pr* was equidistantly distributed in both directions. This characteristic was exploited and the double integration was performed by using a two dimensional version of the Riemman method. A sum over all the values of *x* and θ was performed and then multiplied for *dx* and $d\theta$, this was only possible because the data was evenly distributed in both directions.

```

1 # Perform tomography
2 def tomo(m,phi,x,qMin,qMax,pMin,pMax,density=100,kc=2):
3     global W
4     # Arrays to store data
5     Q = np.linspace(qMin,qMax,density) # q values
6     P = np.linspace(pMin,pMax,density) # p values
7     W = np.zeros((np.size(Q),np.size(P))) # Wigner function
8     # Append the tomography task for all combinations of p and q
9     for q in range(density):
10         for p in range(density):

```

```

11         que.put((q,p,Q[q],P[p],m,phi,x,kc))
12     que.join() # Wait for tasks to be completed
13     return Q,P,W
14
15 # Perform tomography for a fix value of p and q
16 def tomography(iq,ip,q,p,m,angles,x,kc):
17     global W # Variable where W is stored
18     int=0 # Cumulative value of integral
19     # Sum over x and \theta
20     for angle in range(np.size(angles)):
21         argument = m[angle,:] * Kcomp(q,p,angles[angle],x,kc)
22         int += np.sum((argument[1:]+argument[:-1])/2)
23     # Multiply by d\theta and dx and save value
24     W[iq,ip] = int*np.abs(angles[1]-angles[0])*np.abs(x[1]-x[0])
25     /(2*np.pi*np.pi)
26
27 # Perform tomography
28 Q,P,W = tomo(m,phi,x,-5,5,-5,5)

```

Listing A.10: Tomography.

The filtering process took place in the function *Kcomp*. This function decided between using the Taylor approximation on equation [2.68] or the normal expression of the kernel on equation [2.67] based on the value of γ .

```

1 # Kernel
2 def Kor(arg,kc):
3     return (np.cos(kc*arg) + kc*arg*np.sin(kc*arg) - 1)/(arg**2)
4
5 # Taylor approximation of the Kernel using 5 terms
6 def K(arg,kc):
7     return ((kc**2)/2.)*(1-( (kc**2)*(arg**2)/4. )+( (kc**4)*(arg
8     **4)/72. )-( (kc**6)*(arg**6)/2880. )+( (kc**8)*(arg**8)
9     /201600. ))
10
11 # Choosing when to use Taylor
12 def Kcomp(q,p,angle,x,kc):
13     turn = 0.01 # Gamma value
14     # The argument for the Kernel is calculated
15     arg = ( q*np.cos(angle) ) + ( p*np.sin(angle) ) - x
16     # If the value of the argument is greater than gamma the
17     # kernel is computed normally otherwise the Taylor
18     # approximation is used
19     arg[np.abs(arg*kc)<turn] = K(arg[np.abs(arg*kc)<turn],kc)

```

```

16     arg[np.abs(arg*kc)>=turn] = Kor(arg[np.abs(arg*kc)>=turn],kc)
17     return arg

```

Listing A.11: Filtering.

The Wigner function was plotted using the following code

```

1 fig = plt.figure(dpi=200)
2 ax = fig.add_subplot(111, projection='3d')
3 X, Y = np.meshgrid(P,Q)
4 ax.set_ylabel(r"$q$")
5 ax.set_xlabel(r"$p$")
6 ax.set_zlabel(r"$W(q,p)$")
7 ax.plot_surface(X, Y, W, rstride=1, cstride=1, cmap="viridis",
8                  edgecolor='none')
9 ax.xaxis.set_pane_color((1.0, 1.0, 1.0, 0.0))
10 ax.yaxis.set_pane_color((1.0, 1.0, 1.0, 0.0))
11 ax.xaxis._axinfo["grid"]['color'] = (1,1,1,0)
12 ax.yaxis._axinfo["grid"]['color'] = (1,1,1,0)
13 ax.zaxis._axinfo["grid"]['color'] = (1,1,1,0)
14 plt.savefig("number",dpi=300)
15 plt.close()

```

Listing A.12: Plot Wigner function.

A.3 Density matrix calculation

The density matrix in the quadrature representation can be obtained using Eq. 2.69. This integral was performed using function *wignerToRho*, which receives the matrix where the data of the Wigner function is going to be stored, and two arrays that indicate the values of *q* and *p*.

```

1 # Obtains rho qq from wigner function
2 def wignerToRho(w,q,p):
3     # Arrays to store data
4     normQ = np.empty(np.size(q)*np.size(q))
5     primQ = np.empty(np.size(q)*np.size(q))
6     rhoQQ = np.empty(np.size(q)*np.size(q))
7     k=0 # index
8     # Loop all values of q
9     for i in range(np.size(q)):
10         for j in range(np.size(q)):
11             # get rho positions
12             normQ[k] = q[i]+q[j]
13             primQ[k] = q[i]-q[j]

```

```

14     # Integrate
15     int = w[i,:]*np.exp(2j*p*q[j])
16     rhoQq[k] = np.abs(np.sum((int[1:]+int[:-1])*np.abs(p
17     [1:]-p[:-1])/2))
18     k+=1
19     # Return rho qq in 1d arrays
20     return rhoQQ,normQ,primQ
21
22 # rho qq in from Wigner function
23 rho,q,qp=wignerToRho(W,Q,P)

```

Listing A.13: Rho matrix reconstruction.

The density matrix in the Fock representation was obtained using Eq 2.70 using the density matrix in the quadrature representation. As the result of the algorithm to obtain the ρ_{qq} returned non organized equidistant data, two approaches were considered. The first one was to interpolate data and the second one to performed a gaussian fit. The first approach is general and works for any state, the second approach is only for gaussian like ρ_{qq} . All the states tested in this work had a gaussian shaped ρ_{qq} .

```

1 # Interpolate rho qq usig cubic splines
2 def rhoInterpolate(rho,q,qp,qmax,qmin,density=100):
3     # Get data in limits
4     index = np.logical_and(np.logical_and(q>qmin,q<qmax),np.
5     logical_and(qp>qmin,qp<qmax))
6     rho,q,qp=rho[index],q[index],qp[index]
7     # Perform interpolation
8     f = interpolate.interp2d(q, qp, rho, kind='quintic')
9     # Generate new space
10    x,y = np.linspace(qmin,qmax,density),np.linspace(qmin,qmax,
11    density)
12    # Obtain values of rho in new space
13    rho = f(x,y)
14    # Return new space and rho
15    return x,y,rho
16
17 # Interpolated rho qq
18 q,qp,rho = rhoFitting(rho,q,qp,np.max(Q),np.min(Q))

```

Listing A.14: ρ_{qq} interpolation.

```

1 # 2d Definition of a gaussian function
2 @jit(nopython=True, parallel=True)

```

```

3 def gauss2d(t, amp, muX, muY, sigX, sigY, theta):
4     x,y = t
5     a = (np.cos(theta)**2)/(2*sigX**2) + (np.sin(theta)**2)/(2*
6         sigY**2)
7     b = -(np.sin(2*theta))/(4*sigX**2) + (np.sin(2*theta))/(4*sigY
8         **2)
9     c = (np.sin(theta)**2)/(2*sigX**2) + (np.cos(theta)**2)/(2*
10        sigY**2)
11    f = amp*np.exp(- (a*((x-muX)**2) + 2*b*(x-muX)*(y-muY) + c*((y-
12        muY)**2)))
13    return f.ravel()
14
15
16 # Fit rho qq to gaussian function
17 def rhoFitting(rho,q,qp,qmax,qmin,density=100):
18     # Get data in limits
19     index = np.logical_and(np.logical_and(q>qmin,q<qmax),np.
20         logical_and(qp>qmin,qp<qmax))
21     rho,q,qp=rho[index],q[index],qp[index]
22     # Perform fitting
23     arguments, variance = curve_fit(gauss2d, (q,qp), rho, p0=[1, q
24         [np.argmax(rho)], qp[np.argmax(rho)], 0.7, 0.7, 0], bounds
25         =([0,-100,-100,0.05,0.05,0],[10,100,100,100,100,2*np.pi]))
26     # Generate new space
27     x,y = np.linspace(qmin,qmax,density),np.linspace(qmin,qmax,
28         density)
29     X,Y = np.meshgrid(x,y)
30     # Obtain values of rho in new space
31     rho = gauss2d((X,Y),arguments[0],arguments[1],arguments[2],
32         arguments[3],arguments[4],arguments[5]).reshape(density,
33         density)
34     # Return new space and rho
35     return x,y,rho
36
37
38 # Fitted rho qq
39 q,qp,rho = rhoFitting(rho,q,qp,np.max(Q),np.min(Q))

```

Listing A.15: ρ_{qq} gaussian fit.

Once any of these two methods was performed the rho matrix in the Fock basis can be reconstructed. For this the same worker scheme described in appendix A.2 was used, as the values for different n and m are independent.

```

1 # List of tasks to be done
2 queRho = Queue()

```

```

3
4 # Variable to store Rho nm
5 rhoNM = None
6
7 # Define workers
8 def workerRho():
9     # Repeat forever
10    while True:
11        item = queRho.get() # Get tasks
12        quadratureToFock(*item) # Perform task
13        # Inform the queue that a given task was completed
14        queRho.task_done()
15
16 # Number workers, it can be set to two times the number of cores
17 # available in the computer (each processor usually has two
18 # cores)
19 n=8
20 # Create workers
21 for i in range(n):
22     t = Thread(target=workerRho) # Create worker thread
23     t.daemon = True
24     t.start() # Launch worker

```

Listing A.16: Parallelization scheme.

The function that calculated each value of the matrix was *quadratureToFock*, while *rhoFock* filled the task list and returned the full matrix. It required the information of the density matrix in the q representation rho,q,qp, and the limits of *n* and *m*.

```

1 # Calculate a single value of the density matrix in the Fock
2 # representation
3 def quadratureToFock(n,m,rho,q,qp):
4     integral = np.empty(np.size(q))
5     Loop over q values while integrating in qp
6     for i in range(np.size(q)):
7         int = rho[i,:]*np.exp(-0.5*((q[i]*q[i])+(qp*qp)))*
8             eval_hermite(n,q[i])*eval_hermite(m,qp)
9         integral[i]=(np.sum(np.abs(qp[1:]-qp[:-1]))*(int[1:]+int
10            [-1])/2))
11        # integrate over q
12        integral = np.sum(np.abs(q[1:]-q[:-1]))*(integral[1:]+integral
13            [-1])/2)
14        # Multiply by constants and assing values

```

```

11     rhonm[n][m] = integral/(np.sqrt(np.pi*(2**m)*(2**n)*factorial(
12                                     n)*factorial(m)))
13
13 # Calculate Fock matrix
14 def rhoFock(rho,q,qp,n,m):
15     global rhoNM
16     # Varibales to store result
17     rhoNM = np.empty((n+1,m+1))
18     n = np.arange(n+1) # Array on n values
19     m = np.arange(m+1) # Array on m values
20     # Add all values of n and m to the task list
21     for i in n:
22         for j in m:
23             queRho.put((i,j,rho,q,qp))
24     # Wait for all values to be calculated
25     queRho.join()
26     # Return rho matrix in Fock representation and n,m values
27     return rhoNM, n, m
28
29 # Calculate Fock matrix until n=5, m=5
30 rhoNM,n,m = rhoFock(rho,q,qp,5,5)

```

Listing A.17: Quadrature to Fock

Appendix B

GUI

A graphical interface was designed to allow a simpler usage of the program described in the previous appendix. This interface uses the information from marginal distributions, simulated or measured, from files that follow the pattern showcased in Listing A.7. The files to be used can be picked by pressing the buttons next to *Data x*, *Data phi*, and *Data m*. The source code can be found at <https://github.com/amartinez1224/quantum-tomography>.

The GUI allows to intuitively change the tomography parameters and $q-p$ boundaries, select the density of the Wigner function, and select a proper cutoff frequency k_c . Once the parameters are set the *Tomography* button needs to be pressed to start the tomography process.

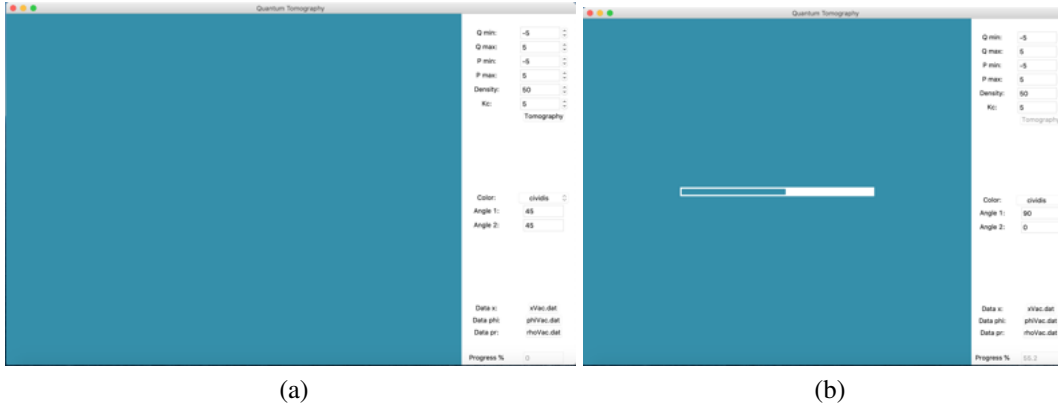


Figure B.1: (a) quantum tomography GUI. (b) GUI while performing tomography.

The interface also allows to set a perspective from where to observe the result, this can be done by changing two angles *Angle 1* and *Angle 2*. Additionally, color settings can be changed. The GUI automatically saves the Wigner function images when generated and allows to save it from different perspectives using the *save* (disc) button.

Furthermore, after performing tomography, the buttons *Density Matrix quadrature* and *Density Matrix Foc* allow to obtain the density matrices in the quadrature an Fock representation of an already generated tomography. These results will open in pop-

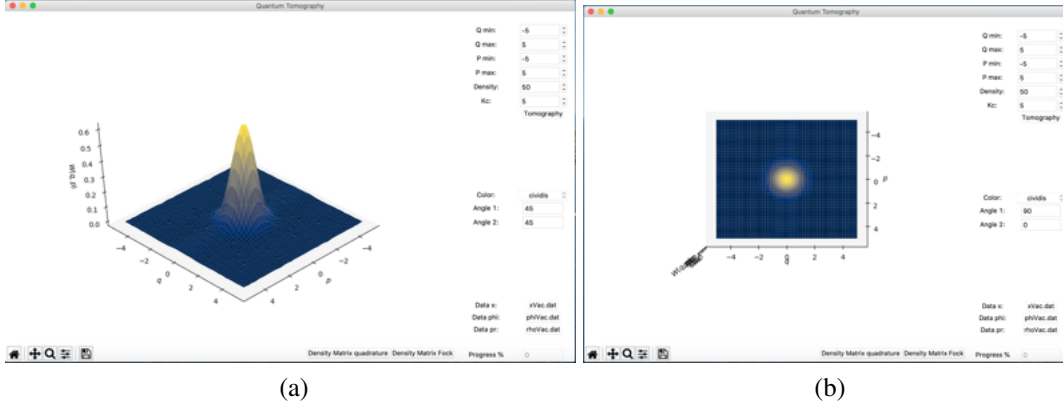


Figure B.2: Tomography results from two different perspectives as portrayed in the GUI.

up windows. The limits of q , q' , p , and p' in the density matrices of the quadrature representation correspond to the same values in which the Wigner function was generated and for the Fock representation n and m values can be given in the pop-up window.

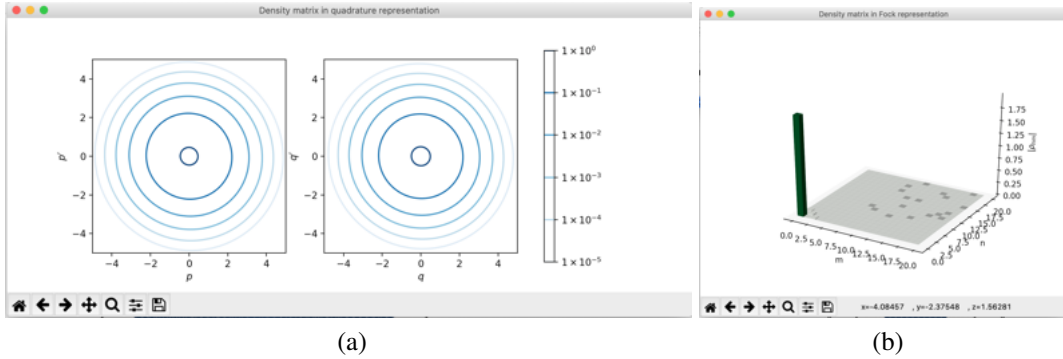


Figure B.3: Density matrices in the quadrature and Fock representation as shown in the GUI. Both results open in pop-up windows.

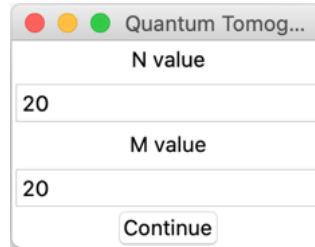


Figure B.4: Set m and n values to calculate the density matrix on the Fock basis.

All the interface can be executed by simply running the script `gui.py`.

INDEX

C

coherent states, [12]

D

density matrix, [12]

density operator, [12]

F

figures, [6–8], [13–18], [20], [22], [25–41], [43–47], [64], [65]

Fock representation, [12]

P

phasor diagram, [5]

photodiodes, [7]

Q

quadrature operator, [11]

quadrature representation, [4]

quadratures, [5]

R

Radon inverse transform, [20]

S

squeezed states, [16]

T

thermal states, [14]

V

vacuum state, [14]